



Microstructure-based fatigue modeling of cast A356-T6 alloy

D.L. McDowell^{a,*}, K. Gall^b, M.F. Horstemeyer^c, J. Fan^d

^a *GWW School of Mechanical Engineering, Georgia Institute of Technology, Atlanta, GA 30332-0405, USA*

^b *Department of Mechanical Engineering, University of Colorado, Boulder, CO 80309, USA*

^c *Materials Mechanics Department, Sandia National Laboratories, 7011 East Avenue, MS 9721, Livermore, CA 94550, USA*

^d *Division of Mechanical Engineering, Alfred University, Alfred, NY 14802-1205, USA*

Received 10 August 2001; received in revised form 29 January 2002; accepted 3 February 2002

Abstract

High cycle fatigue (HCF) life in cast Al–Mg–Si alloys is particularly sensitive to the combination of microstructural inclusions and stress concentrations. Inclusions can range from large-scale shrinkage porosity with a tortuous surface profile to entrapped oxides introduced during the pour. When shrinkage porosity is controlled, the relevant microstructural initiation sites are often the larger Si particles within eutectic regions. In this paper, a HCF model is introduced which recognizes multiple inclusion severity scales for crack formation. The model addresses the role of constrained microplasticity around debonded particles or shrinkage pores in forming and growing microstructurally small fatigue cracks and is based on the cyclic crack tip displacement rather than linear elastic fracture mechanics stress intensity factor. Conditions for transitioning to long crack fatigue crack growth behavior are introduced. The model is applied to a cast A356-T6 Al alloy over a range of inclusion severities.

© 2002 Elsevier Science Ltd. All rights reserved.

Keywords: High cycle fatigue; Microstructure; Cast alloys; A356

1. Introduction

In contrast to conventional strain-life or stress-life approaches for fatigue crack initiation (defined as formation and early propagation to a defect size on the order of 0.5–1 mm), as outlined in the round robin SAE program on a cast A356-T6 Al alloy [31,32], linear elastic fracture mechanics (LEFM) offers a means of introducing microstructure into the correlation/prediction of fatigue life of cast alloys, since the dimension of the life-limiting inclusion serves as the initial size of the crack for the propagation analysis. The application of LEFM is appealing, especially in the high cycle fatigue (HCF) regime, because the behavior of cast Al–Si–Mg alloys, for example, appears to be that of a quasi-brittle material with mode I-dominated crack propagation. However, rather serious limitations of LEFM exist that preclude its use as a quantitative tool for fatigue life prediction for microstructurally and physically small cracks (PSCs) in A356-T6 (cf. [22,23]). Cast A356-T6 is a two-phase Al–Si–Mg alloy, with an Al-rich matrix in dendrite cells reinforced by

* Corresponding author. Tel.: +1-404-894-5128; fax: +1-404-894-0186.

E-mail address: david.mcdowell@me.gatech.edu (D.L. McDowell).

micron-scale Si particles in the eutectic or interdendritic regions. We will refer to any phase that differs from the Al-rich matrix as an “inclusion”, a generalization of the usual metallurgical sense of the word; hence, Si particles, porosity, intermetallics and oxides are all considered as inclusions in this work. Since the matrix is ductile, the local behavior at crack tips encountering inclusions is elastic–plastic. For LEFM to be valid, the scale of the cyclic plastic zone at the crack tip must be small relative to crack length, as must the scale of the damage process zone. Further, for validity of *homogeneous material* solutions for the mode I stress intensity factor, K_I , the cyclic plastic zone must enclose a sufficient number of lower scale inclusions that control the rate of crack advance; this is typically much more demanding than the LEFM requirements on cyclic plastic zone size relative to crack length. The inhomogeneity issue remains even if elastic–plastic fracture mechanics (EPFM) is employed. Even if detailed LEFM solutions are used for local crack geometries forming at lower scale inclusions and growing away from them (cf. [5,18,33]), the ductile nature of the matrix material calls into question the validity of LEFM since even in the HCF regime the local cyclic plastic strain at notches is often substantial. In fact, this point likely renders an overly detailed analysis of stress intensity factors for cracks growing from Si particles or moderate size gas-driven or shrinkage-driven pores more of an academic than practical exercise; even if interaction effects of the crack with other adjacent inclusions are considered, LEFM is based on linear elastic solutions that invoke the small scale yielding assumption.

For small fatigue cracks with length from tens to hundreds of microns in cast alloys, treatment of closure effects within the context of an idealized LEFM approach based on ΔK_{eff} is difficult to justify in view of the heterogeneity of the material, plastic deformation, and multiple crack closure processes.

We present here a model that spans the HCF and low cycle fatigue (LCF) regimes in cast A356-T6 Al alloy. Crack *incubation* at inclusions (particles, casting pores) is assumed to be comprised of a crack nucleation phase and a phase associated with propagation within the influence of the micronotch root field. The complexity of these two phases is modeled using a modified Coffin–Manson relation based on the notch root average cyclic plastic shear strain amplitude, determined from finite element analyses of fractured and debonded particles and pores of various sizes. The small crack growth behavior is modeled using a dependence on the cyclic crack tip displacement (ΔCTD). The ΔCTD accounts for the effects of microstructure heterogeneity. As shown by [28], the propagation of small cracks (in the range of 0.1–1 mm) in two squeeze cast Al–Si alloys (crack formation controlled by Si particles, minimum porosity) for $R = \sigma_{\text{min}}/\sigma_{\text{max}} = -1$ followed an EPFM law that was valid for steels as well [26,35], i.e.,

$$\frac{da}{dN} = A \left(\frac{\Delta\sigma}{2S_u} \right)^n a \propto \Delta\text{CTD} \quad (1)$$

where a is the crack length, N is the number of cycles, S_u is the ultimate strength and A , n ($n = 4.8$ for their Al–Si alloys) are constants. The range of crack tip displacement at some distance in the wake of the crack tip (a few μm) is denoted by ΔCTD . McDowell and Bennett [24] argued that this type of relation may be expected based on shear strain localization ahead of the crack tip, with the cyclic crack tip opening displacement regime as the governing parameter for crack extension (see also [20]), even under HCF conditions for small cracks. A similar relation is adopted in this work.

A criterion is offered for the transition from small fatigue crack growth to long crack behavior; the latter is characterized by sufficient sampling of microstructure within the crack tip damage process zone and is therefore governed by LEFM, so long as the applied stress is below net section yielding. Finally, an effective final crack length concept is developed to address the multisite incubation, propagation and coalescence of fatigue cracks in the bulk of cast alloys under LCF conditions. Rather nonintuitive results are obtained for fatigue resistance in the LCF and HCF regimes for large and small defects, respectively; specifically, small, finely distributed inclusions such as Si particles lead to much lower LCF resistance than a material with larger pores. The converse is true in the HCF regime. Examples are provided for a horizontally cast A356-T6 Al alloy.

2. Multiple regimes of fatigue crack development and growth

Fig. 1 shows a schematic of three distinct regions of the constant amplitude, completely reversed uniaxial strain- and stress-life plots for a low porosity A356-T6 alloy. In this plot, the length scale ‘ D ’ pertains to the diameter of a typical Si particle or a small pore for the case of significant gas-driven microporosity (referred to here as “gas pores”). The length scale ℓ pertains to the size of the plastic zone at the notch root, defined as the scale over which the local plastic shear strain meets or exceeds 0.01%. Effectively ℓ , gives a length scale over which local maximum cyclic plastic strain concentration is “substantial”, defined in an *arbitrary* but *consistently applied* manner. Here, we restrict the values of ℓ to lie in the range $0 \leq \ell \leq D$, such that we regard the case $\ell \rightarrow D$ as a limiting case of unconstrained plasticity associated with macroscopic yielding and ultimately extensive plasticity. Computational micromechanics studies were conducted over a substantial range of inclusion geometries (pores and Si particles) and size distributions to determine the notch root average value of the maximum local cyclic plastic shear strain amplitude, $\beta = \Delta\gamma_{\max}^p/2$, as a function of the applied strain amplitude [10]. Similar studies were carried out to examine the effects of nearest neighbor distance and proximity to the free surface [7]. The matrix elastoplasticity is assumed to conform to

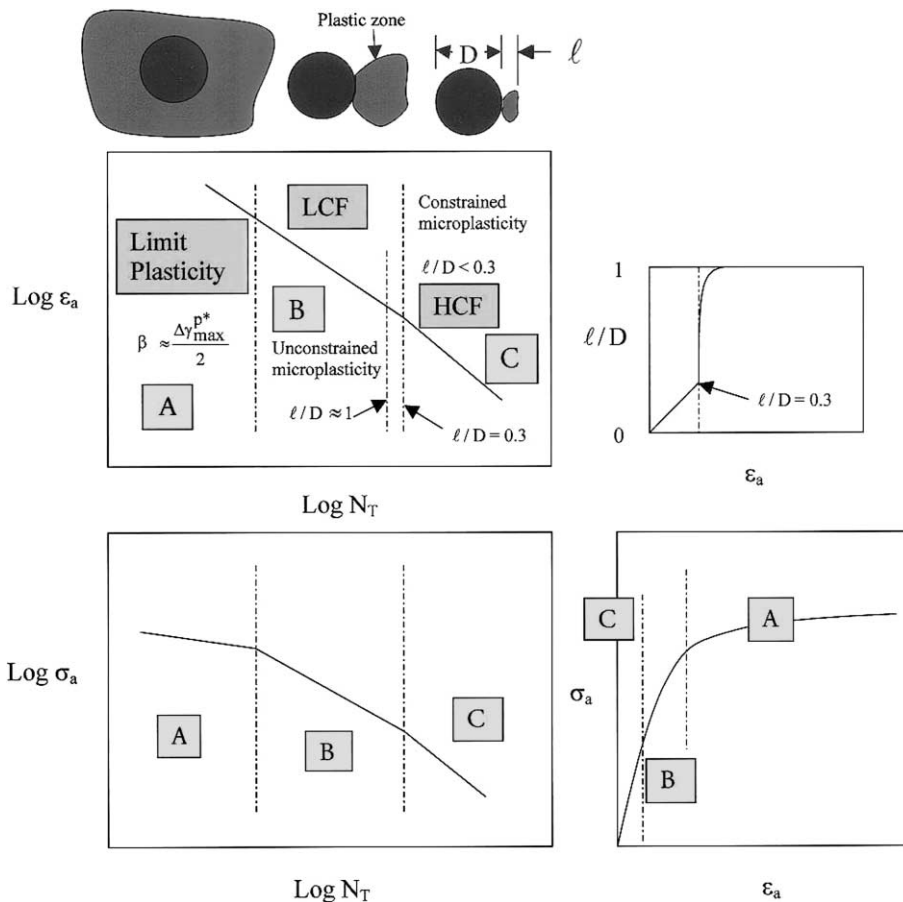


Fig. 1. Regimes characterizing cyclic microplasticity at Si particles and casting pores: (A) EPFM propagation dominated, (B) transition regime, (C) incubation dominated. Here, D is the inclusion diameter and ℓ is the cyclic plastic zone size.

experimental cyclic stress–strain behavior of Al–1%Si specimens, the in situ dendrite composition, tested at room temperature and a frequency on the order of 1–10 Hz. Nonlinear kinematic hardening plasticity theory with linear dynamic recovery was employed (cf. [21]).

With the particle spacing being on the order of particle diameter in the eutectic regions and $\ell/D < 0.3$, the local plasticity at cracked/debonded particles or gas pores is confined to the vicinity of the inclusion and does not interact strongly with neighboring inclusions. We term this regime as constrained microplasticity. Interestingly, for pores or debonded Si particles, the value of $\ell/D = 0.3$ approximately corresponds to the macroscopic cyclic yield strength of A356-T6, so we can connect the transition from microplasticity to macroscopic plasticity (hysteresis in the global cyclic stress–strain response) as that from constrained plasticity to unconstrained plasticity within the microstructure. We may regard $\ell/D = 0.3$ as a percolation limit for microplasticity through the microstructure. The regime of limit plasticity sets in as ℓ/D approaches unity, i.e. the plasticity becomes extensive and the macroscopic state of cyclic plasticity as measured on test specimens is virtually indistinguishable from the microplasticity. Constrained microplasticity exists below the macroscopic yield point and leads to the formation and growth of small fatigue cracks. The applied uniaxial strain amplitude for the yield point of A356-T6 is approximately $\varepsilon_a \approx 0.0023$, which corresponds to the percolation limit for microplasticity ($\ell/D \approx 0.3$) and the point of demarcation between LCF and HCF.

At applied strain amplitudes well above the percolation limit, a condition of limit plasticity is reached in which the remote, average plastic strain amplitude approaches the order of the local plastic strain amplitude within the microstructure. Both eventually exceed the remote applied elastic strain amplitude at an applied strain amplitude of about 0.008. This distinction from the conventional definition of HCF and LCF in wrought alloys (i.e., equality of elastic and plastic strain amplitudes) is significant. For A356-T6, the HCF region according to our definition is beyond about 5×10^4 cycles, whereas according to the conventional definition, it is beyond only 100 cycles for this alloy. It is likely that high strength wrought alloys with fine scales of heterogeneous microstructure are subject to similar categorization, as their conventional transition fatigue lives are often on the order of tens or hundreds of cycles.

In view of the fatigue sensitivity to bulk defects for cast alloys, a hierarchical approach is adopted for modeling inclusions (crack nucleation sites). Cast Al–Si–Mg alloys manifest heterogeneity at several length scales. The dendrite cell size (DCS), or spacing of the secondary dendrite arms, is typically on the order of 20–70 μm , depending on the solidification rate. The Si particle size distribution ranges from about 2 to 10 μm , with extreme particles as large as 15 μm . The aspect ratio of particles may be as high as 1.5–2. Particle size and shape depends on cooling rate, heat treatment, and alloying modification. The eutectic composition of the metal matrix within the interdendritic regions is roughly Al–1% Si. Strong particle–matrix interfaces tend to promote particle strengthening in these alloys. The grain size is much larger, often on the order of millimeters, and is consequential only to the extent of secondary correlations with shrinkage porosity. Trapped gas pores may be very small in dimension and relatively uniformly distributed in interdendritic regions for relatively high cooling rates, assuming moderate values of hydrogen in the melt, or may be as large as 15–50 μm for isolated pores for slower cooling rates. Normally, small gas pores have a mild aspect ratio. Shrinkage-driven pores (referred to here as “shrinkage pores”) develop complex, tortuous shapes in connection with contraction of material during freezing which drives the motion of the gas–fluid interface. Although gas pores also exhibit local shrinkage, shrinkage pores are generally larger and less subject to hydrogen precipitation effects. Typically, the minimum radius of curvature of shrinkage pores with diameter greater than the DCS is on the order of 1/3–1/2 the DCS. Shrinkage pores are often as large as 200–600 μm in thick section castings. Shrinkage porosity and the growth of gas porosity can be eliminated or minimized by squeeze casting. Hot isostatic pressing is a technique to close down porosity following solidification. Other principal types of casting inclusions in Al–Si–Mg alloys include intermetallic particles and oxides. Intermetallic particles may be finely dispersed within the microstructure (cf. [8]); fatigue surface metallography indicates that a higher fraction of the fracture surface follows such particles, at high crack tip driving forces. Whether to treat them as inclusions or as effectively modifying the fracture

resistance of the matrix is problematic. We choose the latter for simplicity and clarity. On the other hand, surface oxides which enter with the molten metal flow always act as brittle inclusions [1]. Above a certain size, they essentially behave as cracks when loaded normal to their long axes.

A hierarchical treatment of five inclusion types is proposed here, with size spanning the range of length scales listed below, according to the order of ascending severity:

Type	Inclusion
A	Distributed microporosity and Si particles; no significant pores or oxides
B	High levels of microporosity; no large pores or oxides (length scale of <3DCS which is about 60–300 μm)
C	Large pores (length scale > 3DCS)
D	Large pores within one pore diameter of the free surface; no large oxides (length scale > 3DCS)
E	Large folded oxides (length scale > 3DCS)

The hierarchical approach to fatigue modeling of cast alloys permits bypass of certain crack growth regimes associated with lower length scales if the cracks incubate at larger defects. These bypass relations will be quantified later in the paper. The total fatigue life is modeled as the sum of numbers of cycles spent in several consecutive stages as follows:

$$N_T = N_{\text{inc}} + N_{\text{MSC}} + N_{\text{PSC}} + N_{\text{LC}} = N_{\text{inc}} + N_{\text{MSC/PSC}} + N_{\text{LC}} \quad (2)$$

where N_{inc} is the number of cycles to incubate (nucleation plus small crack growth through the region of notch root influence) of a micronotch root scale crack with initial length, a_i , on the order of 1/2 the maximum Si particle diameter, \hat{D}_{part} , or pore size, \hat{D}_p . Here, N_{MSC} is the number of cycles required for propagation of a microstructurally small crack (MSC) with length $a_i < a < k$ DCS, where k is a nondimensional factor which represents a saturation limit when the three-dimensional (3-D) crack front encounters a network of Si particles; typically k is 3–5. Further, N_{PSC} is the number of cycles required for propagation of a PSC during the transition from MSC status to that of a dominant, long crack. The long crack propagates according to LEFM with an associated number of cycles N_{LC} . For this alloy, the DCS is typically on the order of 20–100 μm , and the PSC regime may conservatively extend up to 300–800 μm . The model is not limited to these length scales. We discuss them for the purpose of setting a context for interpretation of the model for this particular alloy system. For $a \ll k$ DCS, a significant portion of the 3-D MSC crack front may propagate through the Al-rich matrix within dendrite cells. Since cracked or debonded particles amplify local cyclic plasticity, cracks form there or are attracted towards them because of the intensification of local cyclic plastic strain—however, the crack opening displacement is reduced during particle encounters largely due to crack deflection around particles [7]. A significant fraction of the PSC crack front is engaged in Si particle encounters, advancing intermittently along segments that propagate through cell interiors. However, the crack is sufficiently small such that the stress concentration and cyclic plastic zone ahead of the crack extends only over a fraction of the adjacent cell, e.g. a few Si particle spacings; this depends, of course, on amplitude of applied loading. Hence, there is still an insufficient level of elevated stress ahead of the crack a sufficient distance to debond entire particle/matrix interfaces or to fracture particles; the crack grows by a sequence of successive particle encounters [8,9]. In contrast, a long crack samples enough particles within its crack tip field to uniformly stress and fracture them [8,9]. We heuristically combine the MSC and PSC regimes into a single growth regime for the purposes of modeling, as too little experimental information presently exists to support an intermittent percolation model for the crack front through microstructure in the MSC regime, and it would certainly elevate model complexity.

3. Outline of model

In this section we outline a comprehensive fatigue model for A356-T6 alloy, in ascending order of inclusion severity type, starting with Si particle controlled crack incubation for low porosity castings.

3.1. Type A: distributed microporosity and Si particles; no significant pores or oxides

3.1.1. Incubation

$$\frac{\ell}{D} = \frac{\langle \bar{\epsilon}_a - 0.0006 \rangle}{0.00567} \text{ for } \frac{\ell}{D} \leq 0.3; \quad \frac{\ell}{D} = 1 - 0.7 \left(\frac{0.0023}{\bar{\epsilon}_a} \right)^{1/r} \text{ for } 0.3 < \frac{\ell}{D} \leq 1 \quad (3)$$

where for the argument $\bar{\epsilon}_a - 0.0006$, $\langle \bar{\epsilon}_a - 0.0006 \rangle = \bar{\epsilon}_a - 0.0006$ if $\bar{\epsilon}_a \geq 0.0006$; $\langle \bar{\epsilon}_a - 0.0006 \rangle = 0$ otherwise. The von Mises uniaxial equivalent strain amplitude is defined by $\bar{\epsilon}_a$. In these equations, D is the maximum Si particle diameter in the distribution, $D = \hat{D}_{\text{part}}$. Here, ‘ r ’ is a shape constant for the transition to limit plasticity, which we have taken $r = 0.1$ to provide a rapid transition into the limit plasticity regime as observed in our finite element calculations; $\ell/D \approx 0.95$ at a strain amplitude of 0.003. Hence, incubation rapidly becomes an insignificant of the total fatigue life above the percolation limit for microplasticity as extensive shear localization dominates the eutectic regions.

The nucleation of naturally occurring cracks at casting inclusions is related to the local cyclic plastic shear strain through a Coffin–Manson relation for the matrix material (Al–1%Si for A356). Once nucleated, small cracks (typically on the order of a micron) must then propagate through an enclave with a significant gradient of cyclic stress and plastic strain away from the inclusion, typically losing driving force as they grow because they are driven by the intensified local field of the debonded or fractured inclusion. If the driving force remains above threshold, a crack effectively leaves behind the influence of the notch and behaves as a crack with a physical length that includes the inclusion diameter (cf. [6,33]). The micronotch Coffin–Manson law for incubation life (nucleation plus growth within the notch root field) is written in terms of the *notch root averaged* cyclic plastic shear strain amplitude $\Delta\gamma_{\text{max}}^{\text{p*}}/2$ as:

$$\beta = \frac{\Delta\gamma_{\text{max}}^{\text{p*}}}{2} = C_{\text{inc}} N_{\text{inc}}^{\alpha} \quad (4)$$

$$C_{\text{inc}} = C_n + \frac{1}{0.7} \left\langle \frac{\ell}{D} - 0.3 \right\rangle (C_m - C_n) = C_n + z(C_m - C_n) \quad (5)$$

$$C_n = 0.24(1 - \langle R \rangle) \quad (6)$$

Here, C_n is the coefficient for nucleation and small crack growth at inclusions in the HCF regime (constrained microplasticity), and C_m is the Coffin–Manson coefficient for incubation (cycles to formation of a dominant EPFM crack) in the limit plasticity regime (LCF), obtained from the dendrite cell Al–1%Si material. It is intended that the R -ratio in these incubation relations is based on the maximum principal stress. The localization multiplier $z = (1/0.7)\langle \ell/D - 0.3 \rangle$ is nonzero only above the microplasticity percolation limit, and rapidly transitions to unity as the interdendritic plastic shear strain localization sets in just above the microplasticity percolation limit. Beyond this point, the incubation process is negligible (only a few cycles) due to the severe levels of strain localization around particles or pores. The matrix fatigue ductility coefficient is estimated as $C_m = 0.03$, based on LCF experiments on Al–1%Si specimens at lives below 5×10^3 cycles. An additional positive mean stress dependence is embedded in C_n , which reflects an effective decrease in matrix fatigue ductility at higher positive load ratios due to plastic strain localization associated with significant local monotonic plastic shear strain computed on the first half cycle (order of a few % even for applied strain amplitudes of 0.15%); this localized plastic strain level increases with R -ratio

[10]. Furthermore, ratchetting or progressive plastic deformation of the notch root plastic shear strain is also evident in the calculations of [10] and is known to degrade fatigue ductility. The exponent α pertains to the eutectic Al-rich matrix, and is estimated from LCF tests on Al-1%Si as $\alpha = -0.5$. Based on the fit to computational micromechanics solutions below macroscopic yield ($\ell/D < 0.3$), shown in Fig. 2, we write:

$$\beta = \Delta\gamma_{\max}^{p^*}/2 = Y[100\{\bar{\epsilon}_a - 0.00025(1 - R)\}]^{2.45} \tag{7}$$

For debonded particles or pores, the default assumption based on calculated severity [10],

$$Y = (0.1666 + 0.0266R) \tag{8}$$

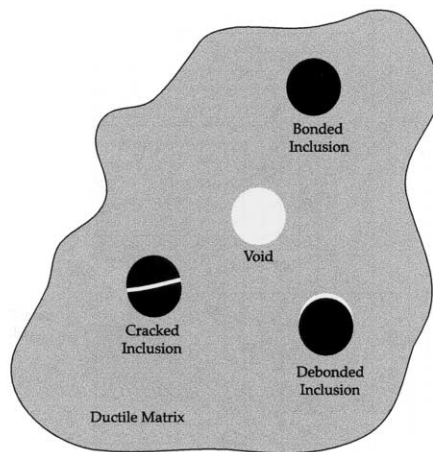
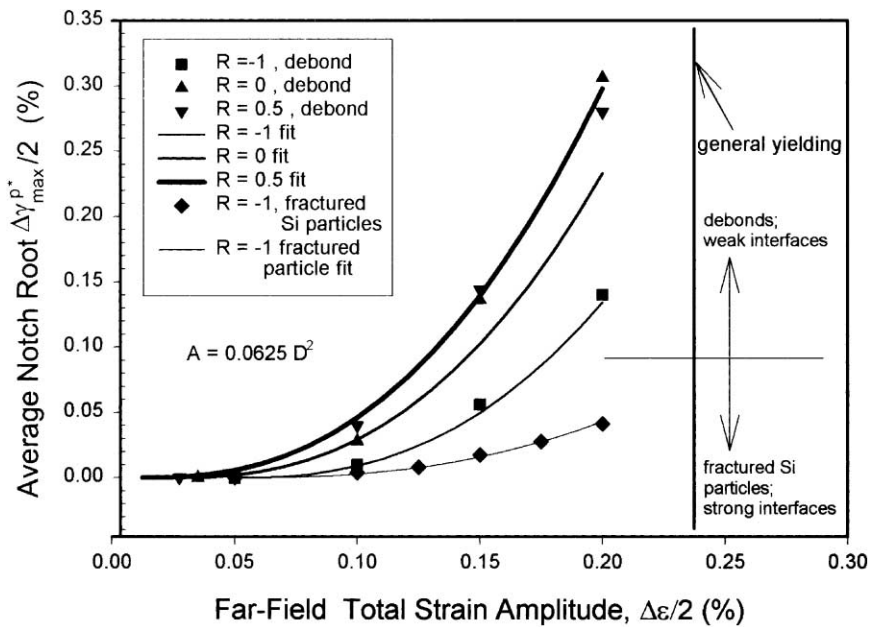


Fig. 2. Correlation of Eqs. (7)–(9) with the FE computational results of [10] for average $\Delta\gamma_{\max}^{p^*}/2$ (in %) versus far-field total strain amplitude, $\epsilon_a = \Delta\epsilon/2$ (in %) for idealized debonded inclusions (Eq. (8), upper curves) and for cracked Si particles (Eq. (9), lower curve). An area of $A = 0.0625D^2$ was used in averaging the cyclic plastic strain in calculations.

For fractured Si particles in case of intact particle/matrix interfaces,

$$Y = 0.32(0.1666 + 0.0266R) \quad (9)$$

For $\ell/D \geq 0.3$, finite element simulations show that β rapidly saturates to a level well above its value at the percolation limit (on the order of 2% plastic strain in the interdendritic regions), i.e.

$$\beta = Y[100\{0.0023 - 0.00025(1 - R)\}]^{2.45}(1 + z\zeta) \quad (10)$$

For debonded particles, the value of $\zeta = 9$ is estimated based on finite element results as $\ell/D \rightarrow 1$, for the $R = -1$ case. Here, ζ is a multiplier on β to represent eutectic strain intensification in the LCF regime. We note that the threshold for β shifts downward with an increase of the R -ratio, evidently in a manner very similar to that described by the Smith–Watson–Topper (SWT) parameter [3]. An increase of the applied peak stress due to an overload drops the threshold level for local microplasticity associated with pre-existing debonds. Since the case of debonded particles is more severe than that of fractured particles in the above relation, and in view of the observation of debonded particles in micrographs, we choose Eq. (8) to define Y .

3.1.2. Propagation

Considering spherical inclusions as a reasonable approximation, the initial crack length is assumed as

$$a_i = \frac{\widehat{D}_{\text{part}}}{2} + \frac{\tilde{\ell}}{4} = 0.5625\widehat{D}_{\text{part}} \quad \text{where } \tilde{\ell} \approx \frac{\widehat{D}_{\text{part}}}{4} \quad (11)$$

In this case, $\widehat{D}_{\text{part}}$ is the largest Si particle diameter from among the population within the highly stressed volume. The length scale $\tilde{\ell}$ corresponds to about a quarter of the particle diameter, based on the averaging the cyclic plastic strain amplitude over a dimension of 25% of the particle diameter at the notch root (i.e., an area of $0.0625D^2$ at the notch root); this also corresponds closely to the percolation limit for microplasticity ($\ell/D = 0.3$). The value $\tilde{\ell}/4$ is about 12.5% of the notch root radius, which corresponds to the Smith and Miller [29] estimate of the transition crack length. Once this length is reached, the crack extends beyond the primary influence of the notch stress field and is in the MSC/PSC propagation regime. This is why we have emphasized that the incubation life from Eq. (4) comprises both crack nucleation and propagation out to the length $\tilde{\ell}/4$. We heuristically assert that formation and early growth of small cracks will span this scale, which includes the difficult-to-treat phenomenon of propagating small cracks through the notch root field (cf. [6,29]). An explicit solution for retardation of the crack tip displacement range for crack growth from micronotches is still not fully developed, since existing solutions for growth from macronotches in otherwise homogeneous material are inappropriate.

The MSC/PSC growth law is given by

$$\left(\frac{da}{dN}\right)_{\text{MSC/PSC}} = G(\Delta\text{CTD} - \Delta\text{CTD}_{\text{th}}) \quad (12)$$

where G is a constant for a given microstructure, typically less than unity (cf. [20]). The threshold value of cyclic crack tip displacement, $\Delta\text{CTD}_{\text{th}}$, is taken on the order of the Burger's vector of the Al-rich matrix; this threshold provides a nonpropagating crack limit which is generally applicable at higher stress levels than the intrinsic threshold limit for cyclic microplasticity associated with incubation. This value is just slightly above the minimum cyclic crack growth rates measured for squeeze cast Al–Si alloys [27,28]. Plumtree and Schafer [27] reported the minimum crack growth rate for cracks blocked at dendrite cell triple points. The average measured minimum crack growth rates should be slightly lower, since near threshold the crack front has mobile segments and immobile segments which result in a lower average crack growth rate. Typical fatigue limits reported for cast Al–Si alloys correspond to stress amplitudes that would be

typical of microstructurally small, nonpropagating cracks. They form and grow to a limited extent away from the nucleation sites, but eventually arrest when they lose sufficient cyclic crack driving force according to Eq. (12). The ΔCTD in Eq. (12) is the local value for the MSC/PSC crack and is much lower than the value calculated based on homogeneous LEFM, $\Delta\text{CTD}_{\text{LEFM}} \approx \Delta K^2 / (\pi E S_y)$, because of the tortuous, 3-D crack path of the MSC, with a distribution of pinning points along the front [20]. The threshold is also much lower than the long crack LEFM threshold $(\Delta\text{CTD}_{\text{LEFM}})_{\text{th}}$, and in principle represents the effect of lattice friction. We assert that when the local value of ΔCTD is used, the irreversibility factor G is on the order of that for long cracks, in the range of 0.3–0.5 (cf. [17,20]); it would be much lower (perhaps two orders of magnitude) if the macroscopic $\Delta\text{CTD}_{\text{LEFM}}$ were used. Hence, cyclic crack advance above threshold is about 1/3–1/2 of ΔCTD .

The Si particles are expected to control fatigue crack growth for eutectic propagation in the MSC regime [8,9]. At high applied strain amplitudes (and longer crack lengths), particle/matrix decohesion and even particle cracking is extensive enough over a larger fraction of the population of Si particles such that the cracks tend to grow by an overload mechanism, which is an entirely different mode of propagation from the MSC regime in the early stages of HCF. In HCF specimens we observed particle cracking only at longer crack lengths; for cracks less than a few hundred microns in length we observed Si particle debonding along the fracture path in HCF loading [8]. We must introduce both modes of propagation into the da/dN versus ΔCTD relation in Eq. (12) by incorporating the change of mechanism through an applied strain amplitude (or ℓ/D) dependence. Accordingly, we introduce the form

$$\Delta\text{CTD} = f(\bar{\varphi}) C_{\text{II}} \left(\frac{\text{DCS}}{\text{DCS}_0} \right) \left[\frac{U \Delta\hat{\sigma}}{S_u} \right]^n a + C_{\text{I}} \left(\frac{\text{DCS}}{\text{DCS}_0} \right) \left(\Delta\gamma_{\text{max}}^{\text{p}} / 2 \Big|_{\text{macro}} \right)^2 \quad (13)$$

The first term is based on the correlations of Shiozawa et al. [28] for cracks in the MSC/PSC regime under HCF loading conditions, with an additional influence of average void volume fraction (porosity) $\bar{\varphi}$ via the function $f(\bar{\varphi})$ to be discussed later. The second term is added to describe elastic–plastic crack propagation in the limit plasticity regime and represents gross plastic strain driven growth, with C_{I} as the leading coefficient; da/dN is essentially independent of the crack length in this regime, with the macroscopic maximum plastic shear strain amplitude, $\Delta\gamma_{\text{max}}^{\text{p}} / 2 \Big|_{\text{macro}}$, as the driving force. This second term is negligible in the HCF regime as defined by the percolation limit for microplasticity. In Eq. (13), $\Delta\hat{\sigma} = 2\theta\bar{\sigma}_a + (1 - \theta)\Delta\sigma_1$ is the range of the uniaxial equivalent stress, which is a linear combination of the von Mises uniaxial effective stress amplitude $\bar{\sigma}_a \left(= \sqrt{3/2(\Delta\sigma'_{ij}/2)(\Delta\sigma'_{ij}/2)} \right)$ and the range of the maximum principal stress, $\Delta\sigma_1$; θ is a constant factor ($0 \leq \theta \leq 1$) introduced by Hayhurst et al. [15] to model combined stress state effects. Here, C_{II} is a coefficient intended to apply to the MSC and PSC regimes for crack lengths ranging from a few microns to the millimeter range (cf. [14,28]), as long as the crack tip cyclic plastic zone is substantially less than the DCS. The factor U addresses mean stress effects on propagation, which are influenced strongly by interdendritic particle interactions ahead of and in the wake of the crack; $U = 1/(1 - R)$ for $R < 0$, and $U = 1$ for $R \geq 0$, where R (stress ratio) is based on the maximum principal stress. $U = 0$ if the peak principal stress in the cycle is compressive. This form for U is consistent with FE calculations and results of [4]. The exponent $n \approx 4.8$ in the work of [28] is much greater than the usual LEFM value due to the local cyclic plasticity associated with interactions of the crack tip with microstructure heterogeneities. Furthermore, da/dN is linear with crack length in the MSC/PSC regimes early in the HCF life and does not follow LEFM relations. The MSC/PSC growth rate is also linear in DCS as motivated by our FE calculations [7], with DCS_0 being a reference value. Although this is associated with the decreasing constraint on slip with increasing DCS, other influential factors such as Fe-rich intermetallic particle sizes [9,37] and microporosity also may be linked with increasing DCS.

The fatigue limit which corresponds to the threshold condition in Eq. (12), $\Delta\text{CTD} = \Delta\text{CTD}_{\text{th}}$, is almost identical to that proposed by [25] for $R = -1$; it differs slightly for other R -ratios, but the Murakami–Endo

relation is consistent with experimental observations of small crack growth [4] and our calculations for the R -ratio dependence of da/dN .

The role of microporosity (e.g., gas porosity) on fatigue resistance has been cited as a complicating effect on fatigue resistance (cf. [19]), since it is coupled closely with the DCS by virtue of kinetics of microstructure coarsening during solidification. Of course, the level of microporosity is also highly dependent upon the hydrogen gas content in the melt. We assume that the role of microporosity, to be distinguished from $\bar{\varphi}$, is principally to affect cyclic plastic strain localization in the Al-rich matrix within the eutectic regions ahead of the crack tip and in the vicinity of debonds ahead of the crack, thereby contributing to an increase in the Δ CTD, which in turn governs the small crack propagation rate. Recent fatigue data performed on vertically cast specimens [19] revealed that even for very low hydrogen content, the fatigue resistance is enhanced substantially relative to alloys of comparable DCS with higher hydrogen content, even though cracks are observed to form at relatively large shrinkage pores. These results strongly indicate that the fatigue ductility (resistance to forming cracks in the presence of cyclic plastic shear strain) within eutectic regions is effectively compromised by microporosity above a certain threshold level, quite independent of the relation between the DCS and the Δ CTD found in computational simulations in the HCF regime below the microplasticity percolation limit. A combination of 0.1% porosity with a DCS less than $\approx 30 \mu\text{m}$ (representative of fairly rapid solidification rates in thin sections) is an effective threshold level above which the onset of microplastic strain localization affects propagation by diminishing the eutectic matrix fatigue ductility. If the microporosity level is maintained below the 0.1% threshold, then larger DCSs can be admitted (longer solidification times) while still maintaining good fatigue ductility of the eutectic matrix. Above this threshold, differences between fatigue life as a function of the DCS are due to effects of the DCS on the constraint of the Δ CTD in the MSC/PSC propagation law. From an engineering standpoint, the tentative conclusion is that when porosity levels exceed $\approx 0.1\%$ within some critically stressed volume, the matrix fatigue ductility degrades significantly. To permit microporosity to decrease matrix ductility, we assign a dependence of the eutectic matrix fatigue ductility in the HCF regime on the average porosity, $\bar{\varphi}$, as a scaling parameter to correlate with the level of microporosity, i.e.,

$$f(\bar{\varphi}) = 1 + \omega \left\{ 1 - \exp \left(-\frac{\bar{\varphi}}{2\varphi_{\text{th}}} \right) \right\}, \quad \varphi_{\text{th}} \approx 10^{-4} \quad (14)$$

Here, ω is a constant on the order of 2–10. The factor of 2–3 reduction in fatigue life observed for higher microporosity relative to low microporosity cast specimens suggests a value of $\omega \approx 2$; a ratio of incubation life to total life of about 1/3 for stress amplitudes in the range of the HCF-transition regime is suggested by the data of [28]. For two different low porosity squeeze cast alloys in the HCF regime, Shiozawa et al. [28] measured the combined coefficient $GC_{\text{II}} = 3.11 \times 10^{-4} \text{ m/cycle}$ for a reference DCS of $\text{DCS}_0 = 30 \mu\text{m}$; in this case, the microporosity is very low, i.e. $f(\bar{\varphi}) \approx 1$.

In the model presented in this paper, *both* microporosity (very small interdendritic pores with dimension significantly less than the DCS) and macroporosity (large shrinkage or gas pores with diameter exceeding several to many times DCS) play a role in reducing the fatigue strength, the former through effective reduction of eutectic matrix fatigue ductility and the latter through reduced incubation lifetimes and larger initial crack sizes for the propagation analysis. The type of small crack growth law of the form given by Eqs. (12) and (13) is consistent with experimental results for cast Al–Si alloys for cracks significantly longer than 1 mm by Shiozawa et al. [28] for stress amplitudes ranging from the vicinity of the fatigue limit to 70% of the ultimate strength (well into the transition regime), so there are no apparent limitations in using Eq. (12) as a good approximation for the growth law of small cracks in small, smooth, uniformly stressed laboratory specimens over essentially the entire life.

We assign the threshold value $\Delta\text{CTD}_{\text{th}} = 2.86 \times 10^{-10} \text{ m} = b$, where b is the Burger's vector for pure FCC Al. This value is just slightly above the minimum cyclic crack growth advance per cycle measured for

squeeze cast Al–Si alloys [27,28]. Plumtree and Schafer [27] reported the minimum crack growth rate corresponding to the blockage of cracks at dendrite cell triple points, where plastic flow on the necessary slip systems for crack advance is suppressed. It should not be surprising that the average measured minimum crack growth rates can even be slightly lower, since near threshold the crack front has mobile segments and immobile segments which result in a lower average crack growth rate.

The cast A356 aluminum alloy considered in this study comprises mainly of a work hardenable aluminum matrix with the major second phase comprising silicon particles in the eutectic region. The aluminum alloy comprised 7% Si, 0.4% Mg, 0.01% Fe, 0.01% Cu, 0.01% Mn, 0.01% Sr, 0.01% Ti, and 0.01% Zn. 20 cm × 14 cm × 5 cm A356 aluminum plates were cast in iron chill molds on the top, bottom, and end of the casting cavity to simulate a permanent mold. A no-bake silica sand was used to create the sides of the plate, the riser, and the down sprue. A ceramic foam filter was used between the down sprue and the riser. A356.2 ingot was melted in an induction furnace. The melt was grain refined with titanium–boron, strontium modified, and degassed using a rotary degasser. The castings were poured between 950 and 977 K, and then cooled over a 16 h period. The plates were removed from the mold and then heat treated to a T6 anneal (solutionized at 810.8 K for 16 h, quenched in hot water at 344 K, and then aged for 4 h at 427.4 °F). The microstructure contained aluminum-rich dendrite cells, equiaxed fine silicon particles distributed in the interdendritic regions, and sub-micron intermetallics. Samples were excised from these castings.

For horizontally cast A356-T6 plate, we take $G = 0.32$ and the other nondimensional constants that result from data correlation give $C_I = 0.31$, $C_{II} = 1.88 \times 10^{-3}$, $n = 4.8$ (as in [28]), and $\omega = 2$. The reference DCS value is assumed as $DCS_0 = 30 \mu\text{m}$, corresponding to the horizontally cast plate. For horizontally cast plate, S_u is 310 MPa. The exponent $n = 4.8$ is also reasonably close to the exponent on stress range of the da/dN versus ΔK relation for the A356-T6 alloy in the long crack regime, and is supported by limited finite element calculations of the Δ CTD versus applied stress for cycling in the HCF regime [7].

Finally, the long crack LEFM growth relation is given by

$$\left(\frac{da}{dN}\right)_{LC} = A_p((\Delta K_{\text{eff}})^M - (\Delta K_{\text{eff,th}})^M) \quad (15)$$

For A356-T6 (horizontally cast plate), $M \approx 4.2$ and $A_p \approx 1.5 \times 10^{-11} \text{ m}(\text{MPa} \sqrt{\text{m}})^{-4.2}/\text{cycle}$. The intrinsic threshold is given by $\Delta K_{\text{eff,th}} \approx 1.3 \text{ MPa} \sqrt{\text{m}}$ for A356-T6, as determined from the threshold for very high stress ratios. The effective stress intensity factor range is defined by $\Delta K_{\text{eff}} = K_{\text{max}} - K_{\text{op}}$ if $K_{\text{min}} < K_{\text{op}}$, $\Delta K_{\text{eff}} = K_{\text{max}} - K_{\text{min}}$ if $K_{\text{min}} \geq K_{\text{op}}$, where the opening stress intensity factor level is given by

$$K_{\text{op}} = 3.4 + 3.8R^2 \text{ for } R > 0, \quad K_{\text{op}} = 3.4(1 + R) \text{ for } 0 \geq R \geq -1, \quad \text{and } K_{\text{op}} = 0 \text{ for } R < -1$$

as given by Couper et al. [4].

We select between the MSC/PSC and LC growth laws as the crack extends by selecting the maximum of either of the two rates, i.e.

$$\frac{da}{dN} = \max \left[\left(\frac{da}{dN}\right)_{\text{MSC/PSC}}, \left(\frac{da}{dN}\right)_{\text{LC}} \right] \quad (16)$$

subject to a constraint that the requirements for validity of the *homogeneous* LEFM approach to model fatigue crack growth in the heterogeneous cast alloy, as can be approximately expressed by

$$a > 30DCS \left(\frac{S_y}{\Delta\sigma_{\text{eff}}}\right)^2 \quad (17)$$

where $\Delta\sigma_{\text{eff}} = \sigma_{\text{max}} - \sigma_{\text{op}}$. This criterion corresponds to a cyclic plastic zone enclave at the crack tip on the order of the DCS. A MSC/PSC to long crack transition in growth behavior corresponding to Eq. (17) was

observed experimentally [8,9]. For stress amplitudes on the order of the cyclic yield strength, S_y , this crack length is on the order of 1 mm for typical DCS, and increases for lower stress amplitudes. The validity limits of LEFM are otherwise less stringent (e.g., the ratio of the cyclic plastic zone to the crack length is small) in the HCF regime.

Finally, we sum the various components of lifetime as follows:

$$N_T = N_{inc} + N_{MSC/PSC} + N_{LC} \quad (18)$$

3.2. *Type B: high levels of microporosity—shrinkage or gas pores with maximum diameter $\widehat{D}_p < 3DCS$ but greater than the maximum Si particle diameter, \widehat{D}_{part}*

3.2.1. Incubation

This case is the same as for Type A inclusions in Section 3.1, except the relevant definition of maximum inclusion diameter D is the maximum pore diameter, i.e. $D = \widehat{D}_p$.

3.2.2. Propagation

The same analysis applies as for Type A inclusions in Section 3.1 with the exception that the initial crack length is given by

$$a_i = \frac{\widehat{D}_p}{2} + \frac{\tilde{\ell}}{4} = 0.5625\widehat{D}_p \quad (19)$$

3.3. *Type C: large shrinkage or gas pores with diameter $\widehat{D}_p > 3DCS$*

3.3.1. Incubation

The same procedure is used as for Type A or B inclusions except that for $\ell/D < 0.3$,

$$\beta = \Delta\gamma_{max}^{p*}/2 = (0.1666 + 0.0266R)[100\{\bar{\epsilon}_a - 0.00025(1 - R)\}]^{2.45} \left(\frac{\widehat{D}_p}{3DCS} \right) \quad (20)$$

These particles are large enough such that their cyclic plastic notch root strain fields may engulf multiple particles. Hence, the R -ratio dependent threshold is still used for microplasticity, taking into account effects of particle contact or debonds upon unloading and associated plastic strain intensification. The modification involving $\widehat{D}_p/(3DCS)$ is introduced to reflect the linear dependence of the crack opening displacement on the cell size for small cracks (even those under the influence of a large notch root field) growing away from the large pores as determined by the computational micromechanics studies (cf. [7]).

3.3.2. Propagation

The crack propagation analysis is the same as Type A inclusions with the exception that the initial crack size is given by

$$a_i = \frac{\widehat{D}_p}{2} + \frac{1}{2} \left(\frac{DCS}{2} \right) = \frac{\widehat{D}_p}{2} + \frac{DCS}{4} \quad (21)$$

reflecting the fact that the averaging length scale should not continue to increase linearly with the inclusion size, because the minimum radius of curvature of large shrinkage pores with typically tortuous shape is approximately half the DCS. Therefore, a limit is placed on the extent of small crack growth away from pores in the incubation phase, on the order of a fraction of the DCS.

3.4. Type D: large pores near the free surface ($\widehat{D}_p > 3DCS$)

3.4.1. Incubation

This case is analyzed in the same manner as Type C inclusions except that the notch root plastic strain intensification is modified to account for proximity to the free surface according to a fit to finite element simulations of pores interacting with the free surface [7], i.e.

$$\beta = \Delta\gamma_{\max}^p/2 = \Delta\gamma_{\max}^p/2|_{\text{Type C}} \left[1 + 10 \frac{\ell}{\widehat{D}_p} \exp\left(-\frac{5\chi}{\widehat{D}_p}\right) \right] \quad (22)$$

where χ is the nearest distance of the pore to the free surface. Here, $\Delta\gamma_{\max}^p/2|_{\text{Type C}}$ is the value from Type C analysis of pores. The ratio χ/\widehat{D}_p must be below unity for this correction to be significant, following the computational results. Clearly, the intensification is very significant for large pores very near the free surface, leading to a tremendous decrease in the incubation life relative to interior pores of similar dimension. In fact, fatigue crack nucleation is often assumed to occur at near surface pores [2,8,9,33].

3.4.2. Propagation

The propagation analysis is the same as for Type C inclusions with the exception that the initial crack size is given by

$$a_i = \widehat{D}_p + \frac{1}{2} \left(\frac{DCS}{2} \right) + \chi = \widehat{D}_p + \frac{DCS}{4} + \chi \quad \text{for } \frac{\chi}{\widehat{D}_p} < 1 \quad (23)$$

in order to reflect the fact that the nucleated crack grows rapidly to the free surface, producing a crack on the order of the particle diameter plus the distance to the free surface. Clearly, this very significantly decreases the crack propagation life relative to the previous cases, as is experimentally observed [33].

3.5. Type E: large oxide films

These inclusions are particularly deleterious if they are contiguous and are larger than the largest pore size for $\widehat{D}_p > 3DCS$. In low hydrogen content specimens we examined, 50–100 μm oxide films or plates were found to serve as the initial crack site in many cases when the porosity was insignificant. Of course, oxides and intermetallics are relatively prevalent as “chopped” or small-scale heterogeneities in the Al-rich matrix in the A356-T6 alloy, but this is accounted for implicitly in the coefficients of the crack propagation law.

3.5.1. Incubation

Incubation is negligible as these inclusions act as cracks essentially from the outset. Hence, $N_{\text{inc}} = 0$.

3.5.2. Propagation

Propagation is analyzed in a manner identical to that of Type C inclusions with the exception that the initial crack size is given by

$$a_i = \frac{1}{2} \widehat{D}_{\text{oxide}} \quad (24)$$

where $\widehat{D}_{\text{oxide}}$ is the maximum length of the oxide, presumably projected normal to the direction of the maximum principal stress.

For a given constant amplitude loading condition, the crack growth relations for all Types A–E inclusions can be integrated in closed form. This greatly facilitates implementation and parameter identification.

4. Multisite incubation, propagation and coalescence in LCF

Rather remarkably, the scatter in LCF life for a given applied strain amplitude for cast A356-T6 is almost as large as that in the HCF regime. By contrast, the scatter in fatigue life for wrought alloys in the LCF regime is typically much less significant. This may be understood by virtue of the nature of distribution of crack incubation and propagation in both cases. Under HCF conditions, the fatigue life is controlled by the most severe inclusion and a single, dominant crack normally propagates to failure. Therefore, scatter in HCF is dictated by the extreme statistics of inclusions, namely by the most extreme, life-limiting inclusions within the highly stressed volume. Often, these are present either at or just under the surface for large pores and oxides.

However, as $\ell/D \rightarrow 1$ in LCF, the probability is almost unity for any significant inclusion to form cracks. Hence, the problem of statistical variation shifts entirely to crack propagation from multiple inclusions. Virtually all significant pores can be expected to have a high probability of rapid crack incubation. In addition, the larger, favorably oriented Si particles among the population will fracture (roughly 1% fraction of fractured particles have been observed under tensile loading at 0.5% strain, cf. [12]). Particle fracture begets debonding and formation and propagation of cracks that compete, and potentially interact, with those formed at large pores or oxides. Coalescence of multiple cracks increases the effective growth rate exponentially. Hence, the distributions of large pores, oxides and larger Si particles become critical in considering multisite fatigue damage and coalescence in LCF.

Some authors have applied continuum damage concepts to fatigue of cast alloys with the notion of multisite fatigue damage in mind (cf. [38]). Such approaches consider damage to be continuously distributed. However, we distinguish between the HCF regime in which this sort of approach would not be appropriate and the LCF regime where the approximations involved may become more satisfactory. Monte Carlo numerical simulations may be used to model the growth and interaction of cracks forming at multiple defects, but involve fairly significant idealizations; this is not particularly difficult (cf. [16] for wrought alloys), just time consuming and demanding since detailed characterization of inclusion distributions is required for cast alloys. Instead, we take a simple approach which is aimed more at establishing a lower bound that could be expected for a given average porosity and mean pore size, along with extremal statistics of the spacing of the larger (fractured) Si particles and larger pores/oxides.

The assumption of a dominant crack that propagates from the most severe inclusion might be expected to produce an upper bound (although not a rigorous bound) on the fatigue life for strain amplitudes in the LCF regime (stress amplitudes exceeding the cyclic yield strength). In the HCF regime, experiments [8,10] indicate that the life is indeed limited by the formation and propagation of dominant cracks at the most severe inclusions among the population, often near surface pores. Above the percolation limit for microplasticity as $\ell/D \rightarrow 1$, however, plastic shear strain localization in the interdendritic regions is intense and cracks incubate rapidly. Cracks incubate profusely at all significant pores and the largest Si particles which undergo increasing probability of fracture with increasing strain level, particularly the largest particles among the population with the highest aspect ratios in the direction of the applied principal stress [14]. Since the lifetime is almost entirely propagation dominated in the LCF regime, the basic problem is to track crack growth from various incubation sites in the microstructure. To do this, we use spatial statistics related to nearest neighbors or mean spacing of large pores and particles. The complicating feature of competitive growth processes is convolution of crack growth at different rates from different characteristic incubation sites to track the network of crack advance and eventual coalescence. Here we take a rather simple but effective approach by considering cracks associated with each of these scenarios:

- (a) maximum pore or oxide film size;
- (b) average pore size and spacing;
- (c) maximum fractured Si particle size and spacing.

For a random distribution of pores, the average porosity, $\bar{\varphi}$, is related to the average nearest neighbor spacing between pores, δ_{pore} , of a given average diameter, \bar{D}_p , by the relation [13]

$$\delta_{\text{pore}} = 0.811 \frac{\bar{D}_p}{\bar{\varphi}^{1/3}} \quad (25)$$

where the units of δ_{pore} and \bar{D}_p are in μm . This relation is rigorous for a random (Poisson) distribution, based on the relation of number density to porosity and average particle size. From the stereological work of [12], the fraction of fractured Si particles, f_{part} , is well approximated in tension beyond the percolation limit for cyclic microplasticity by the relation

$$f_{\text{part}} = 0.01 + 0.8(\bar{\epsilon}_a - 0.0023) \quad \text{for } \bar{\epsilon}_a > 0.0023 \quad (26)$$

In view of the arrangement of Si particles in the interdendritic regions and the morphology of the secondary dendrite arms, we consider a 2-D relation for the average spacing between fractured Si particles, δ_{part} , i.e. $\delta_{\text{part}} \propto f_{\text{part}}^{-1/2}$. Specifically, calculations under monotonic tensile loading are fit well by the expression

$$\delta_{\text{part}} = 113 \sqrt{\frac{0.01}{f_{\text{part}}}} \quad (27)$$

where the units of δ_{part} are in μm . The spacing is initially around 120 μm , but reduces to about 90 μm at higher strain amplitudes. For torsion, the relation

$$\delta_{\text{part}} = 113 \sqrt{\frac{0.01}{f_{\text{part}}}} + 107 \quad (28)$$

appears to match simulations reasonably well.

For the evaluation of coalescence, we make several assumptions:

- (a) uniform stress throughout the critically stressed volume;
- (b) constant amplitude loading is applied;
- (c) incubation occurs immediately at all pores and large Si particles, with an initial crack length of half the inclusion diameter;
- (d) the crack growth rate for cracks at each incubation site is proportional to the length of each crack and is well above threshold;
- (e) interaction between cracks prior to joining (propagating together) is ignored.

4.1. Recursion relation for propagation from large pore through a field of Si particles

If a crack forms at a large pore of diameter \hat{D}_p and propagates through a field of fractured Si particles with extremal diameter, \hat{D}_{part} , on the order of the largest Si particles in the distribution and spacing given by δ_{part} in the last section, then the crack will grow more rapidly from the large pore than from Si particles, and will successively coalesce with cracks incubating at Si particles. As the crack lengthens, it will take successively fewer cycles to coalesce due to more time for crack extension from the Si particles in the field. Accordingly, the crack may only have to grow two or three average Si particle spacings before the entire field of cracks coalesce. This motivates the introduction of an effective coalescence crack length for growth from the largest inclusion, which is shorter than the specified final crack length for dominant crack growth, in general. This effective length can be estimated as follows. After initial incubation at all inclusions considered, we must first compute the distance the crack must grow between the large pore and the nearest fractured Si particle in the same number of cycles at the point of coalescence. Since the MSC/PSC

propagation relation is linear in crack length and the stress amplitude is assumed everywhere uniform, the MSC/PSC propagation fatigue life is expressed as $N_{\text{MSC/PSC}} = C' A$, with C' defined as the multiplicative combination of all terms of the first term of the ΔCTD in Eq. (13) (i.e., below limit plasticity) substituted into the crack growth rate relation (12), assuming that ΔCTD is well above threshold. The multiplier A is given by

$$A = \ln \left(\frac{a_{\text{coalesce}}}{a_0} \right) = \int_{a_0}^{a_{\text{coalesce}}} \frac{da}{a} \quad (29)$$

where a_0 is the initial crack length and a_{coalesce} is the final crack length where coalescence (joining) of cracks occurs. We may decompose A into components A_i that represent fractions of lifetime associated with propagation between certain crack lengths, i.e. $A_i = \ln(a_{i+1}/a_i) = \int_{a_i}^{a_{i+1}} da/a$, since $A = \sum A_i$. Defining as $\xi_1 \delta_{\text{part}}$ the distance the crack must grow from the large pore to join with the crack from the first Si particle, and $(1 - \xi_1) \delta_{\text{part}}$ as the distance that the joining crack grows from the particle, it is found from the relation

$$A_1 = \ln \left(\frac{\frac{\widehat{D}_p}{2} + \xi_1 \delta_{\text{part}}}{\frac{\widehat{D}_p}{2}} \right) = \ln \left(1 + 2\xi_1 \frac{\delta_{\text{part}}}{\widehat{D}_p} \right) \quad (30)$$

that

$$\xi_1 = \frac{\widehat{D}_p}{\widehat{D}_p + \widehat{D}_{\text{part}}} \quad (31)$$

such that $1/2 \leq \xi_1 < 1$ is always true if the pore size exceeds the average maximum fractured particle size. During this process, a crack has grown from the second nearest neighbor fractured Si particle by a distance precisely equal to $(1 - \xi_1) \delta_{\text{part}}$. For the next segment of propagation, therefore, the crack from the large pore has an initial length that encompasses half the pore diameter plus the spacing to the nearest fractured Si particle plus $(1 - \xi_1) \delta_{\text{part}}$. It needs only to grow a distance $\xi_2(1 - 2(1 - \xi_1)) \delta_{\text{part}}$ to meet with the crack from the next Si particle that extends a distance $(1 - \xi_2)(1 - 2(1 - \xi_1)) \delta_{\text{part}}$, and so on. Growth continues until a specified final crack length is reached by the largest crack or until widespread coalescence occurs; eventually cracks will join between evenly spaced fractured Si particles ahead of the crack, resulting in spontaneous coalescence over the entire highly stressed volume considered (on the order of the final crack length selected). For the second coalescence step on, $i = 2, 3, \dots, n$, the recursion relation may be written as

$$\xi_i = \frac{\widehat{D}_p^i}{\widehat{D}_p^i + \widehat{D}_{\text{part}}^i}, \quad A_i = \ln \left(1 + 2\xi_i \frac{\delta_{\text{part}}^i}{\widehat{D}_p^i} \right) \quad (32)$$

where

$$\delta_{\text{part}}^i = (1 - 2(1 - \xi_{i-1})) \delta_{\text{part}}^{i-1} \quad (33)$$

$$\frac{\widehat{D}_{\text{part}}^i}{2} = \frac{\widehat{D}_{\text{part}}^{i-1}}{2} + (1 - \xi_{i-1}) \delta_{\text{part}}^{i-1} \quad (34)$$

$$\frac{\widehat{D}_p^i}{2} = \frac{\widehat{D}_p^{i-1}}{2} + \xi_{i-1} \delta_{\text{part}}^{i-1} + 2(1 - \xi_{i-1}) \delta_{\text{part}}^{i-1} + \widehat{D}_{\text{part}}^{i-1} \quad (35)$$

For $i = 1$, we start the algorithm with Eqs. (30) and (31), using the initial pore and particle diameters. $\widehat{D}_{\text{part}}^i$ may be viewed as the effective particle diameter for the next segment of crack growth (it includes all prior crack extension from that particle). Similarly, \widehat{D}_p^i may be viewed as the effective pore diameter at the

beginning of the propagation process for the i th particle coalescence event. As such, the recursion is performed until one of two conditions holds at the n th iterate:

$$\frac{\widehat{D}_p^n}{2} \geq a_f \quad \text{or} \quad \frac{\widehat{D}_{\text{part}}^n}{2} \geq \frac{1}{2}(\delta_{\text{part}} + \widehat{D}_{\text{part}}) \tag{36}$$

where a_f is the maximum specified crack length specified by the user, still within the MSC/PSC regime. Mathematically, we may view the effects of coalescence as effectively contributing to a decrease in the final crack length for a dominant crack propagating from the largest inclusion, in this case a pore. Well above threshold (in either the HCF or LCF regimes below limit plasticity), the lifetime can be expressed for the largest crack as

$$N_{\text{MSC/PSC}} = \left(\sum_{i=1}^n A_i \right) \frac{G \Delta \text{CTD}|_{a=a_f}}{a_f} \tag{37}$$

We may define the *effective final crack length* \tilde{a}_f as

$$\ln \left(\frac{\tilde{a}_f}{a_0} \right) = \ln \left(\frac{\tilde{a}_f}{\widehat{D}_p/2} \right) = \sum_{i=1}^n A_i \tag{38}$$

or more directly as

$$\tilde{a}_f = a_0 \exp \left(\sum_{i=1}^n A_i \right) \tag{39}$$

Since $\sum_{i=1}^n A_i = \ln(\tilde{a}_f/a_0)$ will always be less than $A = \ln(a_f/a_0)$ in the presence of coalescence phenomena, it is clear that $\tilde{a}_f < a_f$, often substantially. This is due to the fact that significant jumps of crack length are realized instantaneously during coalescence events. Close inspection of this recursion relation reveals that if the pore size is relatively close to the particle size, then $\xi_1 \approx 1/2$ and the most dramatic reduction of \tilde{a}_f relative to the specified final crack length, a_f , is realized. In fact, for propagation from a field of monosize particles or pores, the lower bound on \tilde{a}_f is realized as

$$\tilde{a}_f = \frac{\widehat{D}_{\text{part}}}{2} \left(1 + \frac{\delta_{\text{part}}}{\widehat{D}_{\text{part}}} \right) \tag{40}$$

for a field of fractured Si particles, and

$$\tilde{a}_f = \frac{\overline{D}_p}{2} \left(1 + \frac{\delta_{\text{pore}}}{\overline{D}_p} \right) = \frac{\overline{D}_p}{2} \left(1 + \frac{0.811}{\overline{\varphi}^{1/3}} \right) \tag{41}$$

for an average pore diameter of \overline{D}_p . For example, for the case of extremal fractured Si particle sizes of 12 μm , the resulting \tilde{a}_f is only about 54 μm . Typical \tilde{a}_f values for large pores might be on the order of several 100 μm . All of these values result in fatigue lives that are considerably less than would be required for the growth of a dominant crack in the absence of coalescence. Operationally, it is noted that the \tilde{a}_f is simply used in lieu of a_f as the limit of integration in the MSC/PSC crack growth relation, so the coalescence effects are quite conveniently embedded; however, the resulting crack length to be used in subsequent propagation analysis is a_f .

The recursion relation reveals that pores that are large compared to the Si particle size result in $\xi_1 \approx 1$; therefore, in this case the Si particles do not have much effect on reducing the fatigue life because \tilde{a}_f is not reduced nearly to the extent as for $\xi_1 \rightarrow 1/2$.

Finally, the recursion relations can be used when a fatigue crack grows from a large pore through a field of monosize pores that are spaced according to Eq. (25) simply by considering them to play the precise role that the particles played in this formulation. Similarly, we can apply these relations to propagation through a field of Si particles or pores of some average diameter and spacing of a crack originating at an oxide by simply replacing \widehat{D}_p by $\widehat{D}_{\text{oxide}}$.

4.2. Approximation of recursion relation using only initial microstructure geometry

By considering the geometrically compounding recursion relation, a simple series expansion approximation is developed in odd powers of ξ_1 as defined in Eq. (31). This relation has been found to accurate to within 5–10% for \tilde{a}_f over a wide range of ξ_1 values, as demonstrated in Fig. 3 for several relevant cases. For the preceding problem of crack propagation from a large pore through a field of fractured Si particles, it is written quite simply as

$$\tilde{a}_f \approx \frac{\widehat{D}_p}{2} + \frac{(0.685 - 0.04\xi_1)(\xi_1 + 1)}{2} \left(\delta_{\text{part}} + \frac{\widehat{D}_{\text{part}}}{2} \right) \left\{ \sum_{i=1}^n (\xi_1)^{2i-1} + \left(\frac{a_f}{\delta_{\text{part}}} - n \right) (\xi_1)^{2(n+1)-1} \right\} \quad (42)$$

where $n = \text{INT}(a_f/\delta_{\text{part}})$. To apply this relation, it is required that $\delta_{\text{pore}} > \delta_{\text{part}}$, which is the usual case. As before, $1/2 \leq \xi_1 < 1$. The series in this expression is strongly convergent as $\xi_1 \rightarrow 1/2$, but weakly convergent for $\xi_1 \rightarrow 1$; 5–10 terms may suffice for values of ξ_1 up to 0.6, while as many as 40–50 terms may be required for convergence for values near 0.85 or 0.9, in which the recursion relation may be more efficient. The jumps in the \tilde{a}_f values for the recursion relations (solid lines in Fig. 3) are due to the interplay of multiple defect sizes and spacings with coalescence phenomena.

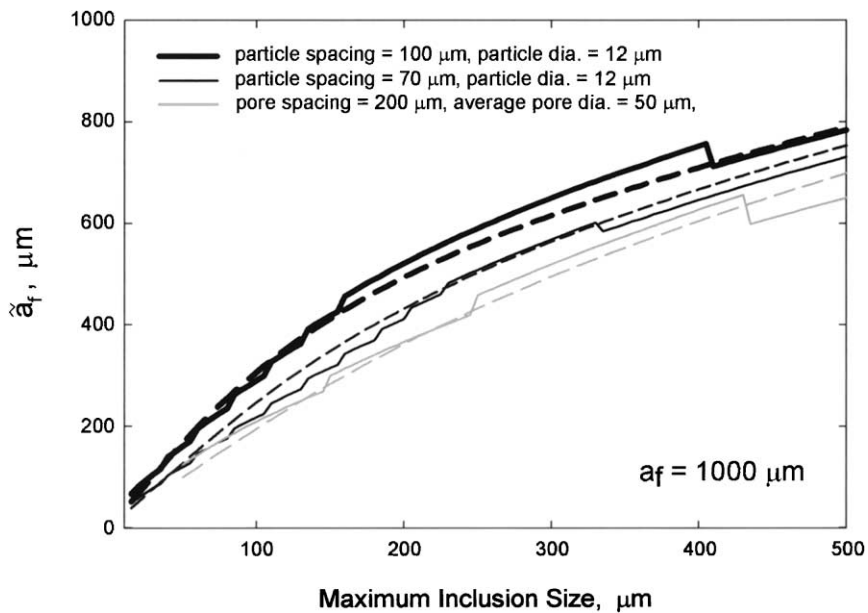


Fig. 3. Effective final crack length versus maximum inclusion (pore) diameter for a specified final crack length of $a_f = 1000 \mu\text{m}$. Solid lines represent results of the recursion relations, while dashed lines represent the approximate series expansion. The top two cases are for a crack growing from pores greater than $12 \mu\text{m}$ in diameter through a field of fractured Si particles spaced either 70 or $100 \mu\text{m}$ apart, while the bottom case is for propagation through a field of monosize pores of $50 \mu\text{m}$ diameter, spaced $200 \mu\text{m}$ apart.

Another application is to consider the accelerative effect of fractured Si particles in-between a field of monosize pores. This can be easily treated by identifying the final crack length as half the averaging pore spacing, i.e.

$$\tilde{a}_f \approx \frac{\hat{D}_p}{2} + \frac{(0.685 - 0.04\xi_1)(\xi_1 + 1)}{2} \left(\delta_{\text{part}} + \frac{\hat{D}_{\text{part}}}{2} \right) \left\{ \sum_{i=1}^n (\xi_1)^{2i-1} + \left(\frac{\delta_{\text{pore}}}{2\delta_{\text{part}}} - n \right) (\xi_1)^{2(n+1)-1} \right\} \quad (43)$$

where $n = \text{INT}(\delta_{\text{pore}}/(2\delta_{\text{part}}))$ in this case. This is not a substantial effect unless the average pore size and Si particle size are of comparable dimensions, with the pore spacing considerably greater than the particle spacing.

As with the full recursion relation, the set of assumptions we have adopted here permit use of only mean microstructure distribution statistics readily obtained from stereology to assess coalescence. In applying these relations, the inclusion diameter must be equal to or exceed the average pore diameter, since extremal inclusions dominate failure. In the absence of pores, Eq. (40) holds. There are no adjustable constants in this formulation beyond these quantitative inputs. Fig. 3 shows the significance of coalescence for cast microstructures with fractured/debonded Si particles, since $\tilde{a}_f \ll a_f$ as the largest inclusion decreases in size. As the maximum inclusion size increases to large values, $\tilde{a}_f \rightarrow a_f$ and the effects of coalescence are much less significant.

5. Model correlations and predictions for horizontally cast A356-T6 plate

5.1. Analysis of dominant defects

Correlations and predictions of smooth specimen uniaxial fatigue tests for horizontally cast plate A356-T6 are presented in this section, with the constants used in Table 1. We assume for these calculations that the final crack size is 1 mm, which is arbitrary but offers a reasonable approximation of total fatigue life for smooth specimens since failure proceeds rapidly in the long crack regime for cracks beyond this length. Hence, $N_T = N_{\text{inc}} + N_{\text{MSC/PSC}}$ since the transition to long crack growth behavior typically occurs in HCF for crack lengths of about 0.7–1 mm. The initial crack length corresponds to each inclusion type as outlined in the model description and is indicated in the legends. In these calculations, we assume that a dominant crack forms at the most severe inclusion and propagates to failure, unassisted by any coalescence with other cracks. The influence of multisite fatigue damage and associated coalescence effects will be examined in Section 5.2, as it is relevant in the LCF regime at stress amplitudes above the macroscopic yield strength. The predictions in Figs. 4–7 are made without considering microcrack coalescence effects, and hence do not address the LCF regime. In the HCF regime, dominant cracks under 1 mm in length are commonly observed (cf. [36]).

Model simulations are shown in Fig. 4 for strain-life and Fig. 5 for stress-life under completely reversed uniaxial loading to a final crack length of $a_f = 1$ mm for various maximum inclusion sizes for horizontally cast A356-T6 plate. In these plots the case ‘50 μm pore’ is a correlation, while all other cases are predictions.

The 200–400 μm pores reduce fatigue life in the HCF regime by factors of roughly 2 and 3, respectively, with greater reductions at amplitudes near the fatigue limit. The predicted fatigue limits for each case are shown with arrows pointing to the right, in each case associated with nonpropagating cracks at the end of the incubation phase. Eliminating the 50 μm pores would result in the particle-dominated incubation enhancement in HCF resistance shown in Figs. 4 and 5. The point where the slope abruptly changes on the strain-life curve corresponds to the percolation limit for microplasticity.

Fig. 6 compares the correlation of horizontally cast plate with 50 μm pores and predictions for various other inclusion scales/types with typical upper and lower bounds of experimental data for various casting

Table 1

Summary of parameter/constant set for horizontally cast plate A356-T6

Stress–strain behavior $K' = 430 \text{ MPa}$, $n' = 0.065$, $E = 71 \text{ GPa}$, $S_u = 310 \text{ MPa}$ Average porosity and pore size: $\bar{\varphi} = 1.5 \times 10^{-3}$, $\bar{D}_p = 45\text{--}50 \text{ }\mu\text{m}$ Maximum pore size: $\hat{D}_p = 50\text{--}55 \text{ }\mu\text{m}$ Maximum Si particle size: $\hat{D}_{\text{part}} = 12\text{--}15 \text{ }\mu\text{m}$ (including effect of aspect ratio)DCS: $\text{DCS} = 30 \text{ }\mu\text{m}$ *Incubation* $C_n = 0.24(1 - \langle R \rangle)$, $C_m = 0.03$, $\alpha = -0.5$ for $\ell/D < 0.3$, $\beta = \Delta\gamma_{\text{max}}^p/2 = Y[100\{\bar{\epsilon}_a - \epsilon_{\text{th}}\}]^q$ for $\ell/D \geq 0.3$, $\beta = \Delta\gamma_{\text{max}}^p/2 = Y[100\{0.0023 - \epsilon_{\text{th}}\}]^q(1 + z\zeta)$, $z = (\ell/D - 0.3)/0.7$ $\epsilon_{\text{th}} = 0.00025(1 - R)$, $q = 2.45$, $\zeta = 9$ $Y = (0.1666 + 0.0266R)$ for debonds $Y = 0.32(0.1666 + 0.0266R)$ for bonded particle/matrix $\ell/D = \langle \bar{\epsilon}_a - 0.0006 \rangle / 0.00567$ for $\ell/D \leq 0.3$ $\ell/D = 1 - 0.7(0.0023/\bar{\epsilon}_a)^{1/r}$ for $0.3 < (\ell/D) \leq 1$, $r = 0.1$ *Propagation*

MSC/PSC regime

 $G = 0.32$, $\Delta\text{CTD}_{\text{th}} = 2.86 \times 10^{-10} \text{ m}$, $C_I = 0.31$, $C_{II} = 1.88 \times 10^{-3}$, $n = 4.8$ DCS₀ = 30 μm , $\text{DCS} = 30 \text{ }\mu\text{m}$, $\theta \approx 0.4$. Microporosity constants: $\omega = 2$, $\varphi_{\text{th}} = 10^{-4}$

Long cracks

 $M = 4.2$, $A_p \approx 1.5 \times 10^{-11} \text{ m}(\text{MPa}\sqrt{\text{m}})^{-4.2}/\text{cycle}$, $\Delta K_{\text{eff,th}} = 1.3 \text{ MPa}\sqrt{\text{m}}$ $K_{\text{op}} = 3.4 + 3.8R^2$ for $R > 0$, $K_{\text{op}} = 3.4(1 + R)$ for $0 \geq R \geq -1$, and $K_{\text{op}} = 0$ for $R < -1$

Constants in boldface are experimentally determined.

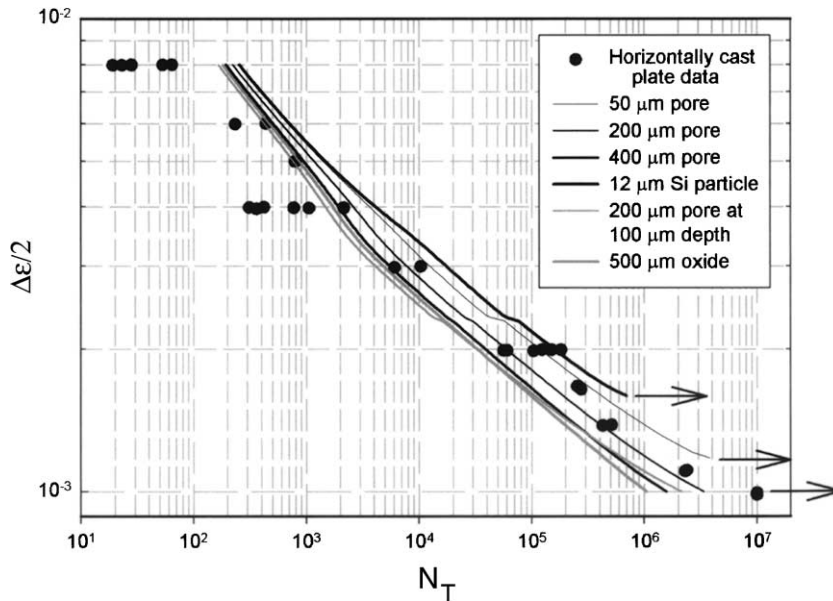


Fig. 4. Model predictions for uniaxial, completely reversed strain-life for incubation at various maximum pore sizes (horizontally cast plate material has a maximum pore size of approximately 50 μm), as well as for the cases of incubation at 12 μm Si particles and 500 μm oxides. Note the drop of fatigue life with maximum pore size, with a strong influence of surface proximity of large pores.

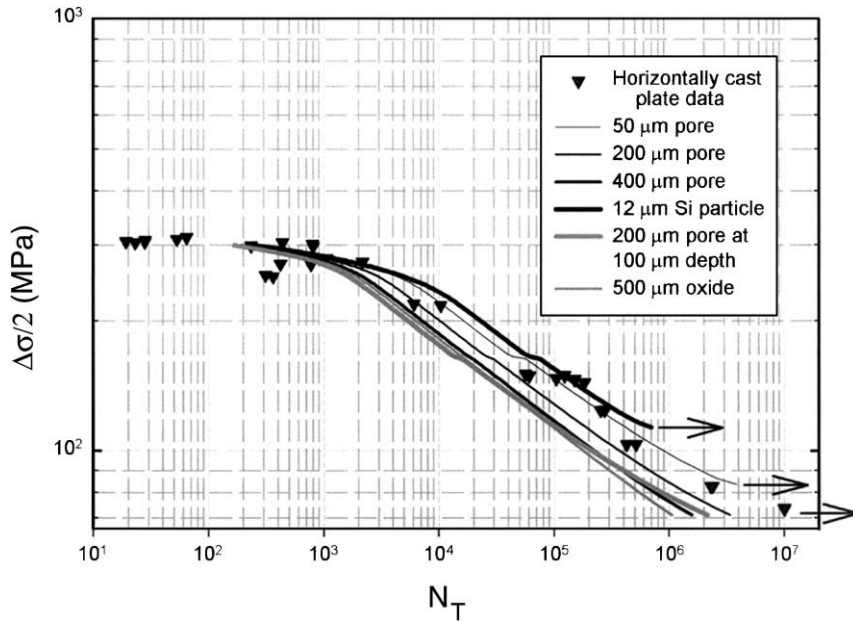


Fig. 5. Model predictions for uniaxial, completely reversed stress-life for incubation at various maximum pore sizes.

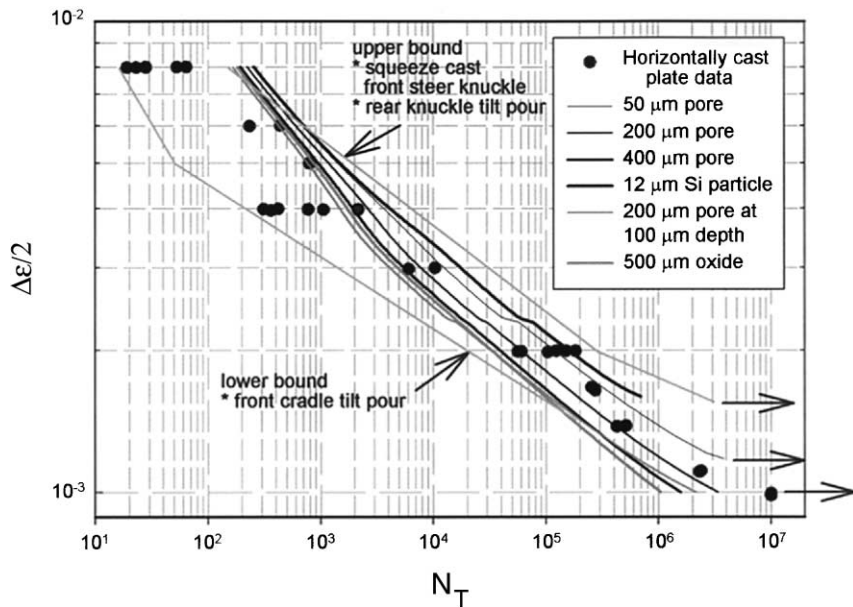


Fig. 6. Strain-life diagram for uniaxial, completely reversed loading for incubation at various inclusion scales/types for horizontally cast plate and comparison with the upper and lower bounds of the strain-life results from the various A356-T6 castings with different as-cast microstructures.

conditions of Al–7%Si alloys. The 400 μm pore results are close to the lower bound in the HCF regime, which had maximum pore sizes of ≈ 500 μm, often occurring near the surface. Of course, the statistical

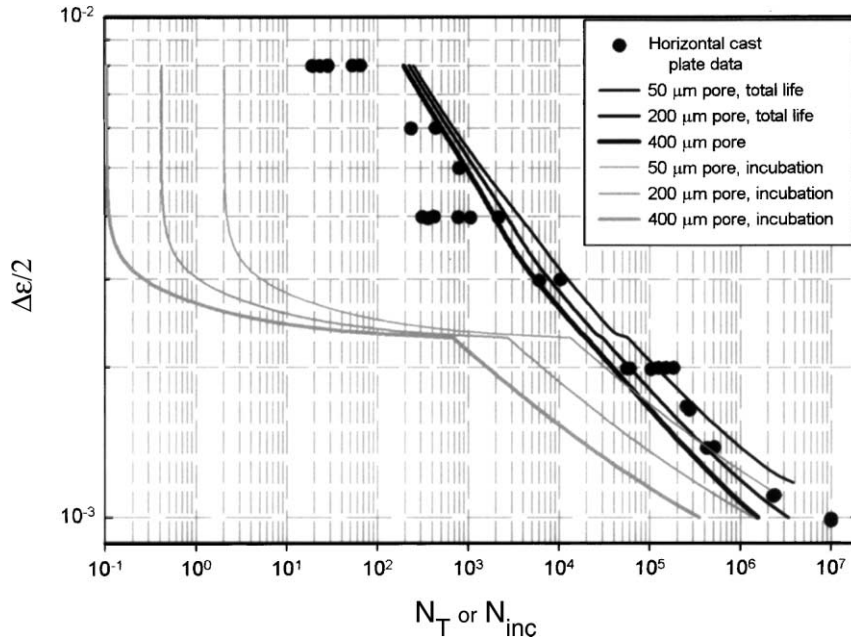


Fig. 7. Strain-life diagram for uniaxial, completely reversed loading for horizontally cast plate with 50 and 200 μm pores, including the crack incubation (light grey lines) as well as the total fatigue life (dark solid lines).

variation in the data in the HCF regime, including that of horizontally cast plate, reflects the variations of the incubating pore (inclusion) size from specimen to specimen. This variability is predicted reasonably well by the model. The upper bound materials are all characterized by low porosity levels (below the threshold $\phi_{th} = 10^{-4}$). It is significant that the predictions in the LCF regime above a strain amplitude of approximately 0.4% are close to an upper bound of the observed fatigue lives due to the neglect of multisite fatigue damage in the microstructure and associated coalescence phenomena in these particular calculations.

To illustrate the relative fractions of incubation life and MSC/PSC propagation life, Fig. 7 shows the curves for incubation life N_{inc} (light grey lines) for maximum pore sizes of 50, 200, and 400 μm . The incubation life is calculated from the relation in Eq. (4) and is clearly negligible in the transition and LCF regimes. However, this is not the case in the HCF regime. Since the growth relation is based on a combination of cyclic crack tip displacement mechanics/calculations and empirical observations, it is conceivable that shielding interactions of small cracks with neighboring Si particles are intrinsic to the model. The incubation life is about 50–70% of the total life in the HCF regime for the 50 μm pores, but only about 20–30% of the total life for 200 or 400 μm pores in the HCF regime. The data of Plumtree and Schafer [27] for A356-T6 for a strain amplitude of 0.18% give an incubation to total life ratio of about 65%, while the predictions here are about 50% at that amplitude for a relatively low porosity casting.

Fig. 8 shows the effects of tensile mean stress on fatigue life for horizontally cast plate in the HCF regime where these effects are of most practical significance. Note that the fatigue limit is reduced very substantially for tensile mean stresses, as are fatigue lives, relative to the completely reversed case. The R -ratio dependence in the model for C_n was selected to fit the 103.5 MPa mean stress case and augments the R -ratio dependence of the local cyclic microplastic shear strain range (Eq. (7) and Eqs. (8) or (9)). Note that the predictions for the other mean stress levels appear reasonable, but there is a paucity of HCF data with mean stress for comparison in view of the inherent scatter. The predictions are very similar to the correlation offered by the SWT parameter (product of the maximum stress and cyclic strain range) applied in

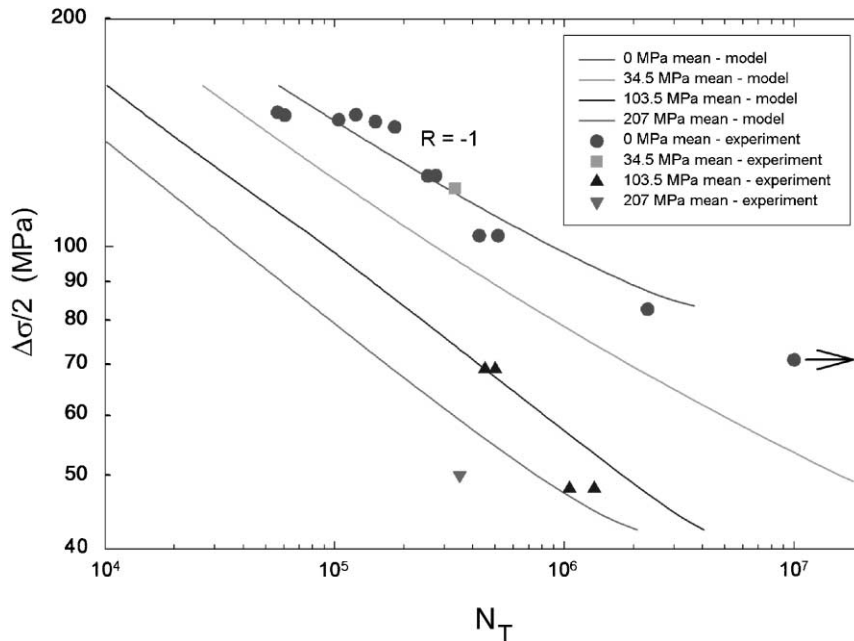


Fig. 8. Mean stress correlations/predictions of model in the HCF regime with horizontally cast plate data for mean stresses ranging from 0 to 207 MPa under uniaxial loading conditions.

strain-life relations. [3] found that the SWT parameter appeared to correlate mean stress effects within the context of a strain-life algorithm relatively well for A356-T6; the SWT parameter is known to describe normal stress-dominated early growth of fatigue cracks in alloys (cf. [22,30]).

The variation of the fatigue life for a given strain amplitude in A356-T6 over a wide range of maximum pore sizes and DCSs is rather well described in the HCF regime using nominal stress-strain, incubation, and propagation properties for the horizontally cast plate; variability in the HCF regime is reasonably well predicted based on the appropriate maximum inclusion size, as shown in Fig. 7. It is likely that the fatigue of this material is strain-controlled, since the incubation phase is dictated by micronotches. It is well known that fatigue of materials with macronotches is a strain-controlled process. Furthermore, the small crack propagation behavior is evidently relatively insensitive to alloy details such as size and distribution of Si particles (cf. [28]).

The model is written in a form that is applicable to multiaxial stress states. The incubation driving force is based on the maximum plastic shear strain amplitude at micronotches, while the MSC/PSC driving force is based on the maximum principal stress range. While the former is based on the local cyclic plasticity that drives small crack formation and growth, the latter is due to the constraint on cyclic crack tip plasticity offered by the Si particles on an otherwise ductile matrix. Future work will consider stress state dependencies based on finite element simulations that include a variation of the applied loading over a broad range of stress states. The current form of the model for combined stress states is therefore subject to modification as these results become available.

We next examine the capability of the existing model, to first order, for multiaxial loading conditions. Completely reversed torsional fatigue experiments on thin-walled tubular A356-T6 specimens from the horizontally cast plate show that the fatigue lives for the cases of uniaxial and torsional fatigue are reasonably well correlated using the Mises equivalent strain for strain amplitudes that are below the percolation limit for microplasticity (for $\ell/D < 0.3$) for final crack lengths of ≈ 1 mm, while torsional specimens

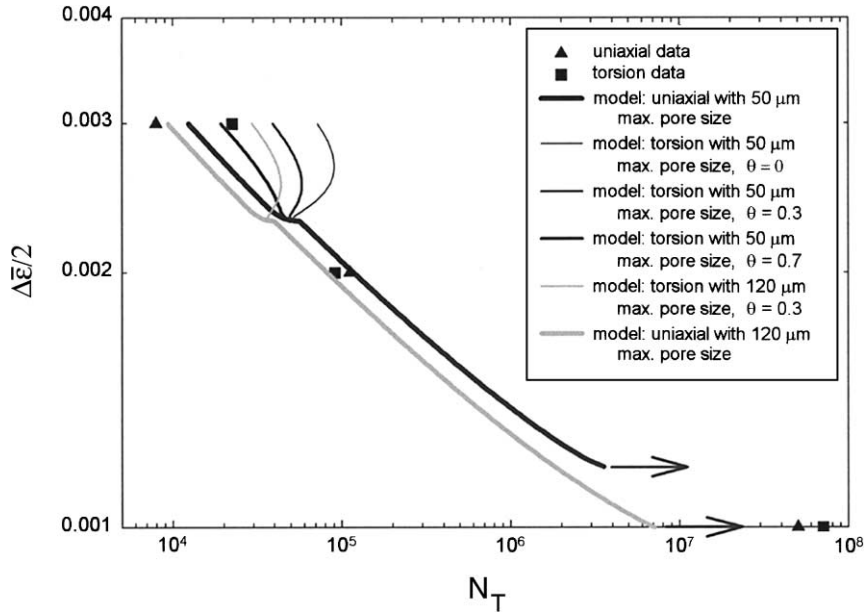


Fig. 9. Comparison of experiments and dominant crack model predictions for completely reversed uniaxial and torsional loading of thin-walled tubular specimens for the horizontally cast plate A356-T6 alloy for several maximum pore sizes and a range of θ values.

are longer lived for strain amplitudes exceeding this level (see Fig. 9). This suggests that the assumption of uniaxial Mises equivalent strain in the incubation driving force is appropriate. It is apparent from Fig. 9 that a value of $\theta \approx 0.4$ in the uniaxial equivalent stress $\Delta\hat{\sigma} = 2\theta\bar{\sigma}_a + (1 - \theta)\Delta\sigma_1$ is necessary to match these results. The ΔCTD is a local mixed mode quantity [31] since it includes the vector magnitude of combined crack tip sliding and opening displacements. The role of the $\Delta\hat{\sigma}$ is to assign a dependence of this mixity on stress state in a phenomenological way, with the magnitudes of $2\theta\bar{\sigma}_a$ and $(1 - \theta)\Delta\sigma_1$ prescribing the relative effects of crack tip sliding and opening, respectively.

5.2. Coalescence and effects of multisite LCF fatigue damage

Here we add the coalescence treatment derived in Section 4 to establish lower bounds on LCF life. This is done by assigning the final crack length for propagation of the most severe (largest diameter) inclusion as the effective final crack length, \tilde{a}_f , in the LCF regime. Accordingly, we assume that

$$\text{Final crack length} = a_f = a_f|_{\text{dominant}} + z \left(\tilde{a}_f - a_f|_{\text{dominant}} \right) \quad (44)$$

where the dominant final crack length is that which is normally assigned in a propagation analysis which assumes a single crack grows to failure, and $z = (1/0.7)\langle \ell/D - 0.3 \rangle$ as before. Since $z = 0$ in the HCF regime, coalescence effects only become significant in the LCF regime for strain amplitudes above 0.0023, the uniaxial yield strain.

Two observations are noteworthy. First, contrasting Fig. 10 with Figs. 4 or 7, it is evident that coalescence is the most likely explanation for the very significant range of fatigue lives observed experimentally in the LCF regime for this material. Multisite fatigue damage has been frequently observed in experiments conducted at amplitudes near the upper range of the HCF region and above. In fact, it is not

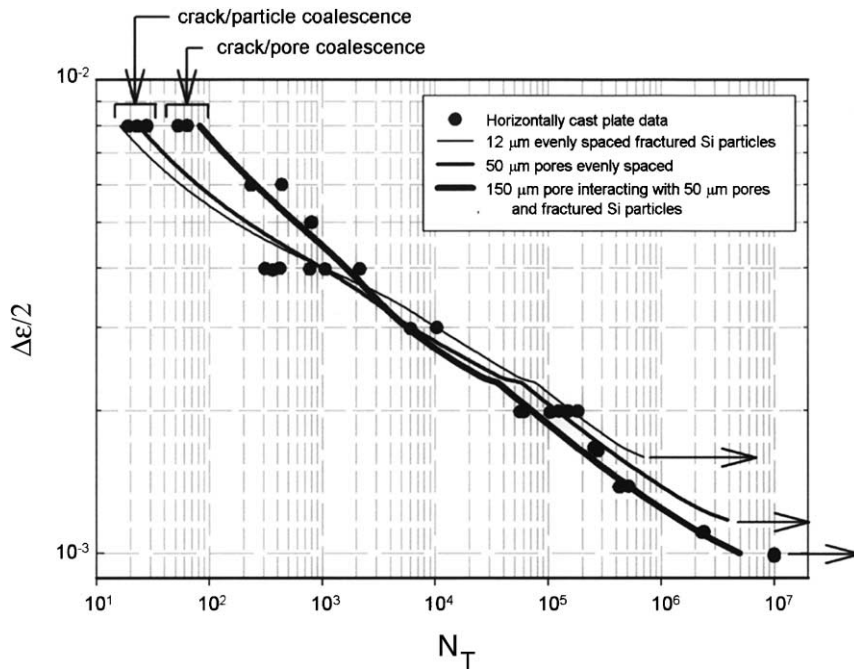


Fig. 10. Variation in completely reversed, uniaxial strain-life behavior as a function of maximum inclusion size for horizontally cast plate, including coalescence effects in the LCF regime. In the coalescence propagation analysis, parameters were assigned as follows based on experimental work: $\bar{\varphi} = 1.5 \times 10^{-3}$, $\bar{D}_p = 50 \mu\text{m}$, $\bar{D}_{\text{part}} = 12 \mu\text{m}$, and $\text{DCS} = 30 \mu\text{m}$.

uncommon to see crack development at multiple sites in HCF, although only one crack typically becomes dominant. Second, a striking result from Fig. 10 is that the case of profuse incubation at the largest Si particles gives the lower bound fatigue life in the LCF regime! This is expected since \bar{a}_f is minimum in this case (see Fig. 3). The fatigue life for the 150 μm pore is much greater, approaching the dominant crack behavior shown in Fig. 4. Therefore, we have an important and somewhat counter-intuitive result from the coalescence analysis: highly refined microstructures appear to offer less LCF resistance than coarse microstructures with higher levels of porosity. The model also predicts that highly refined microstructures (low porosity, small DCS) provide substantial enhancement to HCF resistance relative to coarse microstructures, as observed in the crossover from the LCF regime to the HCF regime for the three cases in Fig. 10, for example. This enhanced HCF resistance is experimentally well documented; near threshold, cracks tend to grow between Si particles in the eutectic regions because most particle–matrix interfaces are intact (cf. [36]). Consequently, it is difficult to tailor a material to achieve both HCF and LCF resistance.

The lack of detailed documentation of variability of fatigue lives in LCF and transition regimes as a function of average and maximum inclusion sites and observed multisite fatigue crack formation and growth likely reflects the rather prevalent bias towards assuming that dominant crack fracture mechanics applies in all cases. In wrought alloys, the variability in LCF response is typically much less than HCF; this analysis suggests that this occurs because the distribution of initial crack sizes in the former is much tighter than the latter.

Fig. 10 also labels the cases of fractured Si particle-controlled coalescence as belonging to a characteristically different set than cases of pore–pore crack interactions. The former form the lower bound LCF behavior, while the latter are intermediate to the dominant crack case, which appear to serve as the upper bound for modeling these experiments.

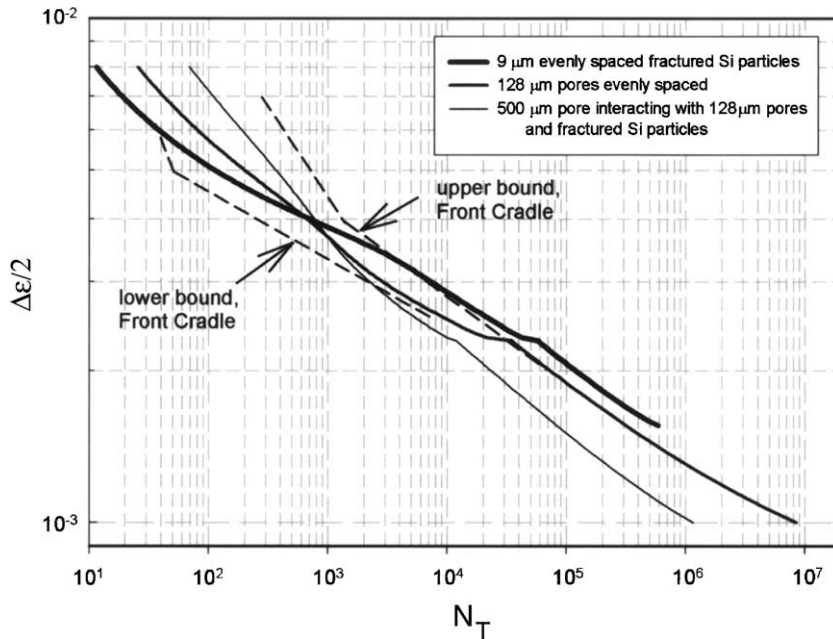


Fig. 11. Estimated variation in completely reversed, uniaxial strain-life behavior of A356-T6 as a function of maximum inclusion size for (top) control arm and (bottom) front cradle, including coalescence effects in the LCF regime. In the coalescence propagation analysis, parameters were assigned as follows based on experimental work: alloy A ($\bar{\phi} = 1.0 \times 10^{-5}$, $\bar{D}_p = 1 \mu\text{m}$, $\bar{D}_{\text{part}} = 6 \mu\text{m}$, and DCS = $25 \mu\text{m}$); alloy B ($\bar{\phi} = 1.1 \times 10^{-2}$, $\bar{D}_p = 128 \mu\text{m}$, $\bar{D}_{\text{part}} = 9 \mu\text{m}$, and DCS = $45 \mu\text{m}$).

The experimentally observed upper and lower bounds on strain-life behavior for A356-T6 over a range of characteristic inclusion severity types are reasonably well described as lying between the dominant crack calculations in Fig. 6 and the lower bound calculations for Si-particle-controlled crack incubation in LCF, as shown for two A356-T6 alloys with a different casting history in Fig. 11. Moreover, the upper and lower bounds in the HCF regime are fairly well predicted using the observed range of maximum inclusion sizes for these materials.

Although the data of any experimental program are necessarily limited and precise statements on upper and lower bounds must be treated with caution, it appears that the following are useful working bounds on fatigue lives for a given constant amplitude loading condition:

HCF (only dominant cracks applicable)

Upper bound: Largest Si particle as crack incubator, porosity $< 10^{-4}$, fine DCS

Lower bound: Largest possible pore or oxide as crack incubator, occurring at or just below the free surface

LCF

Lower bound: Largest Si particle as crack incubator with small crack coalescence; microporosity and larger DCS favored

Upper bound: Dominant, single crack, with largest Si particle as crack incubator producing the longest life

6. Load sequence effects and variable amplitude loading

The present model decomposes the small crack behavior into incubation and propagation components. It can be integrated in closed form for a given material condition (i.e., given DCS, maximum inclusion and pore sizes, microporosity, etc.) and loading condition (constant strain amplitude and stress ratio) to give

$$N_{\text{inc}} = \left(\frac{\beta}{C_{\text{inc}}} \right)^{-2}, \quad N_{\text{MSC/PSC}} = \frac{1}{G\Psi} \ln \left(\frac{\Psi a_f + \Omega - \Delta \text{CTD}_{\text{th}}}{\Psi a_i + \Omega - \Delta \text{CTD}_{\text{th}}} \right) \quad (45)$$

where

$$\Psi = f(\bar{\varphi}) C_{\text{II}} \left(\frac{\text{DCS}}{\text{DCS}_0} \right) \left[\frac{U \Delta \hat{\sigma}}{S_u} \right]^n, \quad \Omega = C_{\text{I}} \left(\frac{\text{DCS}}{\text{DCS}_0} \right) \left(\Delta \gamma_{\text{max}}^p / 2 \Big|_{\text{macro}} \right)^2 \quad (46)$$

If we neglect long crack propagation, then $N_{\text{T}} = N_{\text{inc}} + N_{\text{MSC/PSC}}$. Assume that the rate of incubation damage follows an incrementally linear form (see Eq. (4))

$$\frac{dV}{dN} = C_{\text{inc}}^{-2} \beta^2 \quad (47)$$

where $0 \leq V \leq 1$, and $V(0) = 0$ for undamaged material and $V = 1$ for an incubated crack (at $N = N_{\text{inc}}$); this leads to the result that for constant C_{inc} , the incubation damage is subject the Miner–Palmgren linear damage summation rule, i.e. $\sum n_i / (N_{\text{inc}})_i = 1$ for $i = 1, 2, \dots, N$ loading levels/conditions. Here, n_i is the number of cycles applied under the i th amplitude and R -ratio condition. It remains to be seen how sequences of loading involving excursions above the macroscopic yield point affect the incubation process for subsequent low amplitude cycles, as the literature does not present many results for this type of history for A356-T6. Of particular interest is whether even a few higher amplitude cycles in the transition or LCF regime result in a lasting increase on the rate of small crack formation and growth within the notch root field; if so, then it might be necessary to write

$$C_{\text{inc}} = C_{\text{n}} + \frac{1}{0.7} \left\langle \left(\frac{\ell}{D} \right)_{\text{max}} - 0.3 \right\rangle (C_{\text{m}} - C_{\text{n}}) \quad (48)$$

As a practical matter, above the percolation limit for microplasticity crack incubation is very rapid and so only a small number of cycles are necessary to exhaust the incubation life.

Turning to MSC/PSC crack propagation, almost identical comments apply. As long as (a) Ψ is independent of crack length as framed here, (b) the loading is sufficiently lower than the limit plasticity level such that the effect of the Ω term is negligible ($\Psi a \gg \Omega$), (c) coalescence is neglected, and (d) the driving force is sufficiently above threshold ($\Psi a \gg \Delta \text{CTD}_{\text{th}}$), linear damage summation applies to the MSC/PSC crack growth in the HCF regime as well as up to the limit plasticity regime for given initial and final crack lengths, i.e. $\sum n_i / (N_{\text{MSC/PSC}})_i = 1$. Here, n_i is only the number of cycles applied under the condition of MSC/PSC crack growth and *does not* include cycles involved with crack incubation. The requirement of exceeding threshold is not severe since the driving force depends on a power of 4.8 on the stress range. Again, studies of load sequence effects would shed light on whether periodic LCF excursions are adequately described by the present formulation or whether some permanent memory of overloads should be retained in the crack growth rate relation for lower strain amplitudes. It should be noted that R -ratio effects are introduced in the propagation relation as a modification of the effective stress range and therefore do not contribute to load sequence effects in this relation.

The linear cycle fraction-based damage summation *never applies* over multiple regimes of crack incubation and propagation. It would be inappropriate to argue in favor of linear summation based on the

fraction of N_T , in general. Unfortunately, this is common practice when using strain-life or stress-life approaches for total fatigue life to a crack of a given length such as 1 mm. The nature of damage accumulation is governed by different functions of applied stress and R -ratio in these regimes, fundamentally, and they cannot be combined into one simple summation rule. However, since the equations of the model may be integrated incrementally to give the actual sequence effects, it is unnecessary to introduce ad hoc non-linear damage summation rules. Rather, it is only necessary to include the appropriate amplitude dependent damage mechanisms in the incubation and MSC/PSC crack growth formulations.

At high strain amplitudes in the LCF regime (limit plasticity), Miner's rule again applies because the coefficients of the damage growth rate saturate to the values corresponding to $\ell/D \rightarrow 1$. It is commonly observed that wrought alloys obey Miner's rule for sequences of LCF loading, and the same is predicted for the limit plasticity regime of cast alloys since the influence of particle constraint is lost.

The influence of LCF overloads on the formation of multisite fatigue cracks which may eventually coalesce under lower amplitude HCF loading is an area of uncertainty. Although multiple cracks can form through the microstructure in HCF, only one typically becomes dominant and grows in a manner relatively unaffected by the others until overload conditions are reached. However, periodic excursions of LCF loading may result in multisite incubation and coalescence of fatigue cracks under even subsequent HCF amplitudes, as discussed in a previous section or a random LCF loading excursion may cause coalescence of two dominant cracks that may have not interacted under typical HCF loading conditions. The definition of \bar{a}_f in Section 4 may require revision to account for variable amplitude loading.

7. Transition to long crack fracture mechanics

The fatigue crack growth rate as predicted by the EPFM-based da/dN versus ΔCTD relation in Eqs. (12) and (13) for microstructurally and PSC regimes is generally higher than that based on using LEFM-based relations with constants determined for propagation of mechanically long fatigue cracks. The transition from the small crack growth regime to the long crack growth regime described by Eq. (16) is assumed to occur at the point of crossover of the two rates. Note in Fig. 12 that the value of the effective stress intensity factor range, ΔK_{eff} , at the point of transition to long crack behavior is on the order of $6 \text{ MPa } \sqrt{\text{m}}$, for completely reversed HCF stress amplitudes just above threshold, 90 MPa. This is in close agreement with the value of maximum stress intensity factor of $5.69 \text{ MPa } \sqrt{\text{m}}$ determined by [8] for transition from fatigue crack growth along the interface between Si particles and the Al–1%Si matrix to crack growth through the Si particles that are fractured ahead of the advancing crack.

8. Small and long crack thresholds

The model identifies three kinds of thresholds, in ascending order in terms of applied stress or strain amplitude level:

- microplasticity threshold for crack nucleation—corresponding to absence of cyclic microplasticity at debonded or cracked particles or at pores; a shakedown or lower bound fatigue limit associated with a microplasticity threshold.
- ΔCTD threshold for small crack propagation—corresponding to nonzero cyclic microplasticity below the percolation limit which is sufficient to nucleate cracks at inclusions, but insufficient to propagate the small crack away from the influence of the notch root field, leading to arrested or nonpropagating

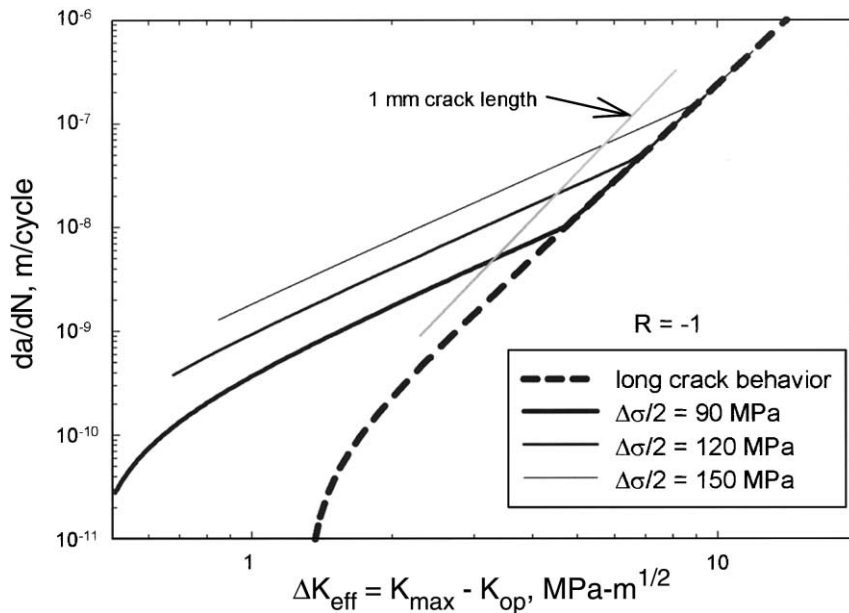


Fig. 12. Plot of predicted da/dN from the model for three constant amplitude, completely reversed stress amplitudes in the HCF regime in terms of the range of the effective stress intensity factor, including transition to long crack behavior where the MSC/PSC and LC growth rates are equal. The labeled light grey line shows the point where a 1 mm crack is reached in the small crack propagation history. The incubation pore size is $50\ \mu\text{m}$ in these calculations. Note that the value of ΔK_{eff} at transition to long crack behavior is on the order of $6\ \text{MPa}\sqrt{\text{m}}$ under HCF conditions, just above threshold.

cracks with length on the order of the inclusion size. Small MSC/PSC cracks incubate in this case but do not continue to propagate out of the influence of the inclusion notch root field.

- long crack da/dN versus ΔK_{eff} threshold, which corresponds to an arrest of the development or coalescence of cooperative elastic–plastic deformation and separation processes that contribute to crack extension for a long crack which samples a statistically homogeneous set of Si particles.

The three thresholds of the present model are shown in Fig. 13 for horizontally cast A356-T6 alloy with a maximum pore size of $50\ \mu\text{m}$. The lowest threshold corresponds to the elastic shakedown limit of cyclic microplasticity within the microstructure without any cracks. The MSC/PSC crack propagation threshold dominates for cracks up to about $400\text{--}500\ \mu\text{m}$, with the LFM propagation threshold relevant to longer cracks holding at lower applied stress levels. The dashed line at $84\ \text{MPa}$ designates an inadmissible boundary because the maximum pore size is $50\ \mu\text{m}$ for the particular case shown.

9. Utility of multiscale model for parametric studies

The model presented in this paper is useful for parametric studies since it explicitly represents the role of various key microstructural descriptors. For example, Fig. 14 shows the computed dependence of total fatigue life to a crack length of 1 mm on inclusion size for three stress amplitudes within the HCF and transition regimes for horizontally cast A356-T6 alloy. Such trend plots may be useful for designing thermomechanical process route in castings as a function of net section and notch root in-service stress levels (cf. [34]).

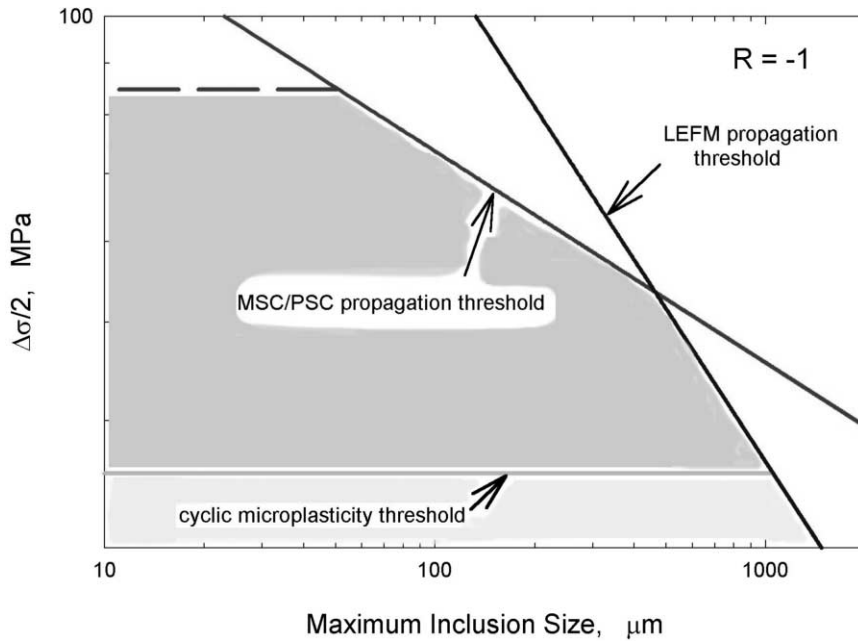


Fig. 13. Kitagawa diagram for completely reversed uniaxial fatigue thresholds constructed from the present model of horizontally cast A356-T6 alloy. In the light-shaded region, cracks do not incubate. In the dark-shaded region, MSC/PSC cracks arrest. The dashed line represents the stress amplitude corresponding to 50 μm average pore diameter. Note that outside the shaded envelopes, MSC/PSC or long cracks can propagate to failure.

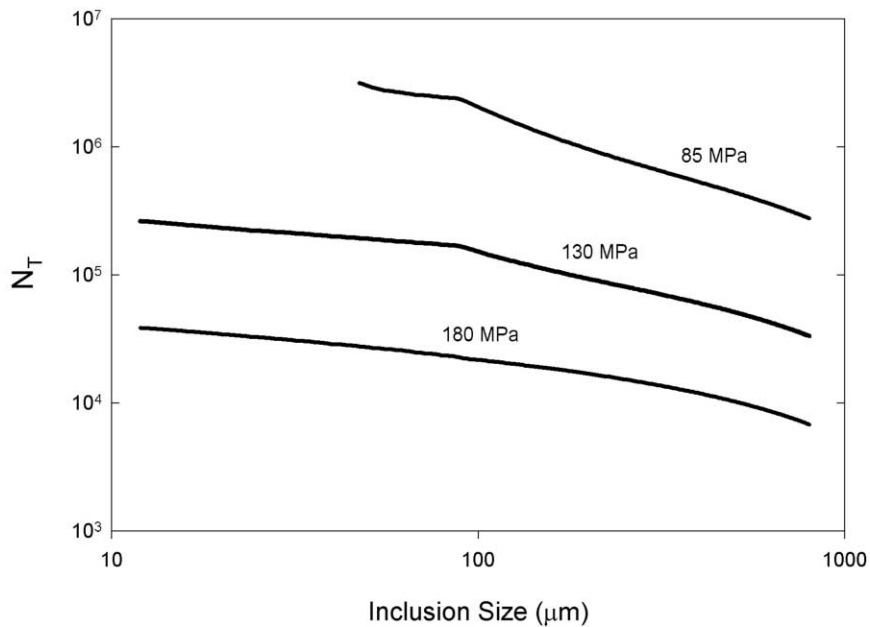


Fig. 14. Example of parametric computational study of total fatigue life (1 mm crack) as a function of completely reversed uniaxial stress amplitude for a wide range of maximum inclusion sizes for horizontally cast A356-T6 alloy.

10. Summary and conclusions

The model proposed in this paper is motivated by a combined set of considerations including physical behavior of A356-T6, quantitative metallography, fractography, and computational micromechanics. Each aspect of the relation of microstructure to fatigue damage is deterministic but has been framed to explicitly incorporate microstructure features, thereby allowing for variability of microstructure to enter naturally and directly into the resulting variability in estimated fatigue life. Hence, the model is amenable to prediction of variability of fatigue life with respect to variation of any particular microstructure feature. Microstructure features include DCS, maximum Si particle size, maximum pore size, maximum oxide size, proximity to the free surface (for large pores), and average porosity level. If the probability distributions of these features are specified based on quantitative metallography, for example, then the probability distributions for the fatigue life can be computed directly from the model.

The model is applied to cast A356-T6 alloy with various types of inclusions, ranging from individual Si particles to large shrinkage pores and trapped oxide films. The model is capable of predicting the variability of fatigue life for realistic ranges of solidification rates, hydrogen gas levels, and resulting microstructures. Three thresholds are explicitly identified in the model, respectively associated with elastic shakedown of the microstructure-scale cyclic plasticity, arrest of incubated cracks at micronotch roots below the percolation threshold, and the usual long crack propagation threshold of LEFM. The transition from HCF to LCF is shown from computational micromechanics to be associated with the percolation limit of cyclic microplasticity within the eutectic regions. A unique coalescence formulation is introduced for multisite damage incubation and growth in the LCF regime. Other features of the model are demonstrated, including multiaxial loading effects, amenability to parametric studies, and capabilities to model sequence effects under variable amplitude loading.

Acknowledgements

The authors are grateful to the American Foundrymen's Society (J. Santner, Program Director) for supporting this model development as part of the overall USCAR-USAMP effort in developing cast alloy technology to enable lightweight vehicle components (Program Managers Richard J. Osborne of General Motors Corporation and Donald E. Penrod of the American Foundrymen's Society). Low porosity vertically cast specimens were obtained from Alcan (F. Major), tested by Westmoreland and then image-analyzed by Dr. Nancy Yang of Sandia-Livermore, all of whom are gratefully acknowledged. The work of M.F. Horstemeyer was performed under U.S. Department of Energy Contract No. DE-AC04-94AL85000.

References

- [1] Campbell J. Invisible macrodefects in castings. *J de Phys* 1993;3(7, part 2):861–72.
- [2] Conley JG, Moran B, Gray J. New paradigm for the design of safety critical castings. In: SAE special publications aluminum in automotive applications, vol. 1350. Warrendale, PA: SAE; 1998. p. 25–38.
- [3] Cordes TS, Berns HD, Lingenseler DJ, Mahoney BJ, Testin RA. A SWT fatigue mean stress model for A356-T6 cast aluminum alloy. In: SAE Technical Publication SP760, Fatigue and fracture toughness of A356-T6 cast aluminum alloy, 881703, 1988. p. 39–48.
- [4] Couper MJ, Neeson AE, Griffiths JR. Casting defects and the fatigue behavior of an aluminum casting alloy. *Fatigue Fract Engng Mater Struct* 1990;13(3):213–27.
- [5] DeBartolo EA, Hillberry BM. Effects of constituent particle clusters on fatigue behavior of 2024-T3 aluminum alloy. *Int J Fatigue* 1998;20(10):727–35.
- [6] Dowling NE. Fatigue at notches and the local strain and fracture mechanics approaches. In: Smith CW, editor. *Fracture mechanics*, ASTM STP 677. Philadelphia: ASTM; 1979. p. 247–73.

- [7] Fan J, McDowell DL, Horstemeyer MF, Gall K. Computational micromechanics analysis of cyclic crack tip behavior for microstructurally small cracks in dual-phase Al–Si alloys. *Engng Fract Mech* 2001;68:1687–706.
- [8] Gall K, Yang N, Horstemeyer M, McDowell DL, Fan J. The debonding and fracture of Si particles during the fatigue of a cast Al–Si alloy. *Metal Mater Trans A* 1999;30:3079–88.
- [9] Gall K, Yang N, Horstemeyer M, McDowell DL, Fan J. The influence of modified intermetallics and Si particles on fatigue crack paths in a cast A356 Al alloy. *Fatigue Fract Engng Mater Struct* 2000;23(2):159–72.
- [10] Gall K, Horstemeyer MF, Degner BW, McDowell DL, Fan J. On the driving force for fatigue crack formation from inclusions and voids. *Int J Fract* 2001;108:207–33.
- [11] Gall K, Horstemeyer M, McDowell DL, Fan J. Finite element analysis of the stress distributions near damaged Si particle clusters in cast Al–Si alloys. *Mech Mater* 2000;32(5):277–301.
- [12] Gokhale AM. Personal communication, 1998.
- [13] Gokhale AM, Personal communication, January 2000.
- [14] Gungor S, Edwards L. Effect of surface texture on fatigue life in a squeeze-cast 6082 aluminum alloy. *Fatigue Fract Engng Mater Struct* 1993;16(4):391–403.
- [15] Hayhurst DR, Leckie FA, McDowell DL. Damage growth under nonproportional loading, ASTM STP 853. Philadelphia: ASTM; 1985. p. 688–99.
- [16] Hoshide T, Socie DF. Crack nucleation and growth modeling in biaxial fatigue. *Engng Fract Mech* 1988;29(3):287–99.
- [17] Kuo AS, Liu HW. An analysis of unzipping model for fatigue crack growth. *Scripta Metall* 1976;10:723–8.
- [18] Laz PJ, Hillberry BM. Fatigue life prediction from inclusion initiated cracks. *Int J Fatigue* 1998;20(4):263–70.
- [19] Major JF. Porosity control and fatigue behavior in A356-T61 aluminum alloy. *AFS Trans* 1994;97-94:901–6.
- [20] McClintock FA. Considerations for fatigue crack growth relative to crack tip displacement. In: Beynon JH, Brown MW, Lindley TC, Smith RA, Tomkins B, editors. *Engineering against fatigue*. Balkema Press; 1999. p. 227–41 [chapter 24].
- [21] McDowell DL. Multiaxial effects in metallic materials. In: *Symposium on Durability and Damage Tolerance*, ASME AD, vol. 43, ASME Winter Annual Meeting, Chicago, IL, 6–11 November, 1994. p. 213–67.
- [22] McDowell DL. Multiaxial fatigue strength. In: *ASM handbook, Fatigue and fracture*, vol. 19. ASM International; 1996. p. 263–73.
- [23] McDowell DL. Basic issues in the mechanics of high cycle metal fatigue. *Int J Fract* 1996;80:103–45.
- [24] McDowell DL, Bennett V. Micromechanical aspects of small multiaxial fatigue cracks. In: *Proceedings 5th International Conference On Biaxial/Multiaxial Fatigue and Fracture*, Cracow, Poland, 8–12 September, 1997. p. 325–48.
- [25] Murakami Y, Endo M. Effect of defects, inclusions, and inhomogeneities on fatigue strength. *Fatigue* 1994;16:163–82.
- [26] Nisitani H. Behavior of small cracks in fatigue and relating phenomena. In: Tanaka T, Jono M, Komai K, editors. *Current research on fatigue cracks*. Current Japanese materials research, vol. 1. Amsterdam: Elsevier; 1987. p. 1–26.
- [27] Plumtree A, Schafer S. Initiation and short crack behaviour in aluminum alloy castings. In: Miller KJ, de los Rios ER, editors. *Behaviour of short fatigue cracks*, EGF Publication, vol. 1. London: Mechanical Engineering Publications; 1986. p. 215–27.
- [28] Shiozawa K, Tohda Y, Sun S-M. Crack initiation and small fatigue crack growth behaviour of squeeze-cast Al–Si aluminum alloys. *Fatigue Fract Engng Mater Struct* 1997;20(2):237–47.
- [29] Smith RA, Miller KJ. Fatigue cracks at notches. *Int J Mech Sci* 1977;19:11–22.
- [30] Socie DF. Critical plane approaches for multiaxial fatigue damage assessment. In: McDowell DL, Ellis R, editors. *Advances in multiaxial fatigue*, ASTM STP 1191. Philadelphia: ASTM; 1993. p. 7–36.
- [31] Stephens RI, Mahoney BJ, Fossman RG. Low cycle fatigue of A356-T6 cast aluminum alloy wheels, SAE Technical Publication SP760, Fatigue and fracture toughness of A356-T6 cast aluminum alloy, 881707, 1988. p. 93–102.
- [32] Stephens RI, Berns HD, Chernenkoff RA, Indig RL, Koh SK, Lingenfeller DJ, et al. Low cycle fatigue of A356-T6 cast aluminum alloy wheels. SAE Technical Publication SP760, Fatigue and fracture toughness of A356-T6 cast aluminum alloy, 881701, 1988. p. 1–28.
- [33] Ting JC, Lawrence Jr FV. Modeling the long-life fatigue behavior of a cast aluminum alloy. *Fatigue Fract Engng Mater Struct* 1993;16(6):631–47.
- [34] Tynelius K, Major JF, Apelian D. A parametric study of microporosity in the A356 casting alloy system. *AFS Trans* 1993;401–13.
- [35] Wang CH, Miller KJ. The effects of mean and alternating shear stresses on short fatigue crack growth rates. *Fatigue Fract Engng Mater Struct* 1992;15(12):1223–36.
- [36] Wang Z, Zhang RJ. Microscopic characteristics of fatigue crack propagation in aluminum alloy based particulate reinforced metal matrix composites. *Acta Metall Mater* 1994;42(4):1433–45.
- [37] Wang QG, Apelian D, Griffiths JR. Microstructural effects on the fatigue properties of aluminum castings. In: *Proceedings 1st International Aluminum Casting Technology Symposium*, Rosemont, Illinois, 12–15 October, 1998.
- [38] Weinacht DJ, Socie DF. Fatigue damage accumulation in grey cast iron. *Int J Fatigue* 1987;9(2):79–86.